UNIVERSITÀ DEGLI STUDI DI PADOVA

Dipartimento di Fisica e Astronomia "Galileo Galilei"

Master Degree in Physics of Data

Final Dissertation

Braiding transitions and plectonemic structures in multiple-stranded chains manipulated by magnetic tweezers

Thesis supervisor

Prof. Enzo Orlandini

Candidate

Filippo Conforto

Academic Year 2021/2022

Abstract

Thanks to the recent advance in micromanipulation techniques based for instance on optical and magnetic tweezers, it is nowadays possible to probe the mechanical response and the configurational transitions of soft structures made by multiple linear polymers, such as ds-DNA filaments, that wrap one to another in a braided fashion. In particular, by using magnetic tweezers one can look at the braided/plectonemic (or buckling) transition of these structures as a function of the extensional force and torsion injected on the system. Recent theoretical and experimental studies have focused on structures made by only two filaments. The aim of this thesis is to extend these investigations to the case of multiple (i.e. more then two) strands where the reciprocal position of the rooted monomers at the tweezeers' plates and the detection of plectonemic structures are interesting novel issues to be explored. Geometric quenches between three-stranded and two-stranded configurations are also explored by introducing a cut along the additional third strand and simulating the system relaxing to equilibrium. The analytical approach is based on the elastic rod model of a chain with bend and twist rigidities, while numerical simulation are performed on a coarse-grained model of three stranded chains whose stochastic dynamics is integrated using LAMMPS code. The study of such new configurations highlights the presence of a buckling transition similar to the one found with two strands, in which the coexistence of plectonemic and non formations is more pronounced than what previously observed. For such phase transition the geometric properties of the system influence directly the critical points positioning.

Contents

Chapter 1

Introduction

The recent advancements in simulative and experimental apparatus were able to unveil new possibilities in biophysics and in particular in DNA physics. Starting from the DNA discovery from Watson and Crick [1], it was possible to investigate more and more the DNA structure, function [2] and the mechanism leading its replication [3]. In particular the presence of supercoiling became one of the central tropic in such studies [4] [5]. Efforts centered mainly on the work done by enzymes such as Topoisomerases [6], allowing to understand more on their role in topology changes during replication, and in particular on their knot solving ability [7].

This interest translated in experiments [8] and simulations [9] [10] aimed at the study of braided configurations of DNA. Part of these efforts focused on a particular phenomenon, the appearance of so called plectonemes [11] and curls in braiding conditions during DNA replication. In this phase the strong tension and torsion induce mechanical instability and the formation of such structures [12].

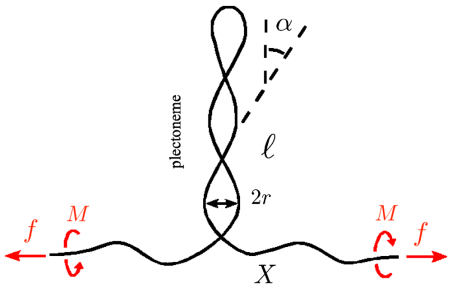

Figure 1.1: Plectoneme example, via [13].

To study these kinds of phenomenons many modelling attempts were done [12] [13] [14], converging to the use of statistical mechanics methods involving free energy minimization. These works focused on the double helix case, involving two strands with fixed persistence length considered as a mean-field helix [14]. Results coming from these analytical models allow predicting the average properties of the braids and the plectoneme formation.

In addition to this, the use of magnetic tweezeers [15] allowed understanding how supercoiling works in different experimental conditions [8]. In fact, these experimental apparatuses allow pairs of strands with fixed ends to be held to a rotating bead and a fixed wall [16]. Within these particular settings the strands, once rotated and braided together, in some conditions of catenation and pulling force undergo to so-called buckling transitions [17], separating two phases, one in which the braid is completely straight and one in which more complex structures develop changing the helix structure, as for example the plectonemes.

Following these experimental efforts, it was also possible to study and reproduce experimental behaviors using computational techniques through the introduction of wormlike chain [18] models, allowing to corse-grain and simulate both single strand and double strand DNA. This was done in previous

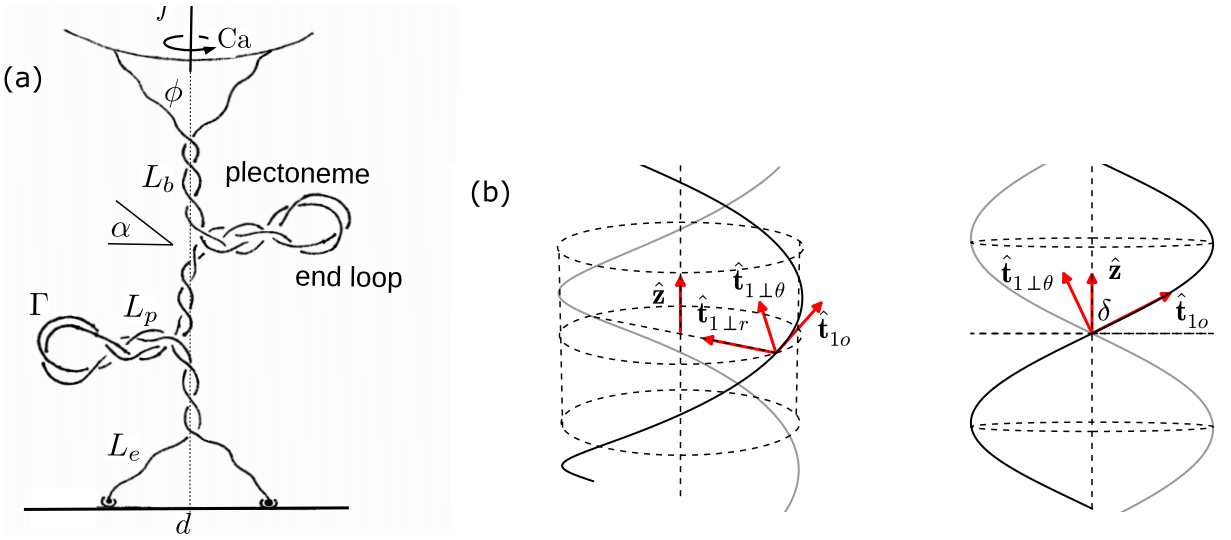

Figure 1.2: Double helix model, via [14].

works [17] by approximating the strands as sequences of beads with fixed size and using molecular dynamics tools such as LAMMPS [19] to rotate them and study the behavior both in equilibrium and in non equilibrium phases.

The aim of this work is to expand the theoretical knowledge of buckling transitions to study more complex systems involving three or more strands [20] with different anchoring configurations. This can be done to improve the knowledge of how DNA can braid in multiple-stranded configurations, while being able to translate such results to more generalized coarse-grained polymers in such conformations. Results obtained during the simulation of such configurations will be discussed and compared to previous works, in particular regarding the plectoneme formation, to study how the statistical mechanics of braiding has changed.

Chapter 2

DNA braiding and magnetic tweezers

The study of DNA under stress and twisting has the main goal to understand the behavior and topology during replication and after the action of topology related enzymes such as topoisomerases Type-I and Type-II. It is possible to verify in experimental setups [21] that such proteins are able to disentangle knotted strands, but also create positive and negative supercoils. These kinds of formations can assume multiple forms, from the more solenoidals ones, to plectonemic structures [11]. These phenomenons were studied and replicated with different techniques, from the use of magnetic Tweezers [8], to the introduction of simulative models with a strong theoretical basis. The more advanced between these models [12] highlighted the presence of a phase transition between an "unbuckled" and a "buckled" phase. In the latter one, the non-braided structures becomes more and more relevant as a way to release the stress through the conversion of the twist into the writhe (see appendix B). Within this phase it is possible to characterize the plectoneme statistics with adequate models, while the use of advanced apparatuses such as magnetic tweezers makes possible to observe experimentally the supercoils formation and the strand behavior.

2.1 Analytic approaches

These experimental and qualitative efforts where then followed by more analytic ones, involving the introduction of free energy and mean field models [13] [14]. One of the most successful approaches for the two-strands case involves the modelling of a mean field helix, parametrized by ξ, the dimensionless arclength, $\mathbf{r_i}(\xi)$ and $\mathbf{t_i}(\xi)$, that are respectively the position vector and the tangent to the mean field helix, for the two parts of the helix. These ideal helixes represent the single strands of the braids in an approximated fashion, allowing to study the energy terms for the interaction between the strands.

With these premises it is possible to introduce a general Hamiltonian for the couple of strands, considering each possible interaction force.

$$\beta\mathcal{H} = \int_0^{\frac{L}{A}} d\xi \left[\frac{1}{2} \left(\left| \frac{d\hat{\mathbf{t}}_\mathbf{1}}{d\xi} \right|^2 + \left| \frac{d\hat{\mathbf{t}}_\mathbf{2}}{d\xi} \right|^2 \right) \right] - \frac{\beta A f}{2} \hat{\mathbf{z}} \cdot \left(\hat{\mathbf{t}}_\mathbf{1} + \hat{\mathbf{t}}_\mathbf{2} \right) + \mathbf{U}(\mathbf{r_1}, \mathbf{r_2})$$

The first term is associated to the energy of local curvature of the two strands, while the second one is associated to the pulling force applied to the extremities of the DNA molecule, with f the pulling force and A a scaling factor. The last term is instead related to the electromagnetic potential of self-electromagnetic interactions and interactions between two different strands [22].

Further approximations along the tangent vector of the strands and the use of fourier transforms allows to simplify the expression and get an approximation of the total free energy as a sum of components, each one associated to different parts of the braid. These are the mean field free energies $\beta\mathcal{E}_s$, $\beta\mathcal{E}_p$ and their relative fluctuations $\beta\Delta\mathcal{F}_s$, $\beta\Delta\mathcal{F}_p$, that once summed correspond to the total free energy of such system.

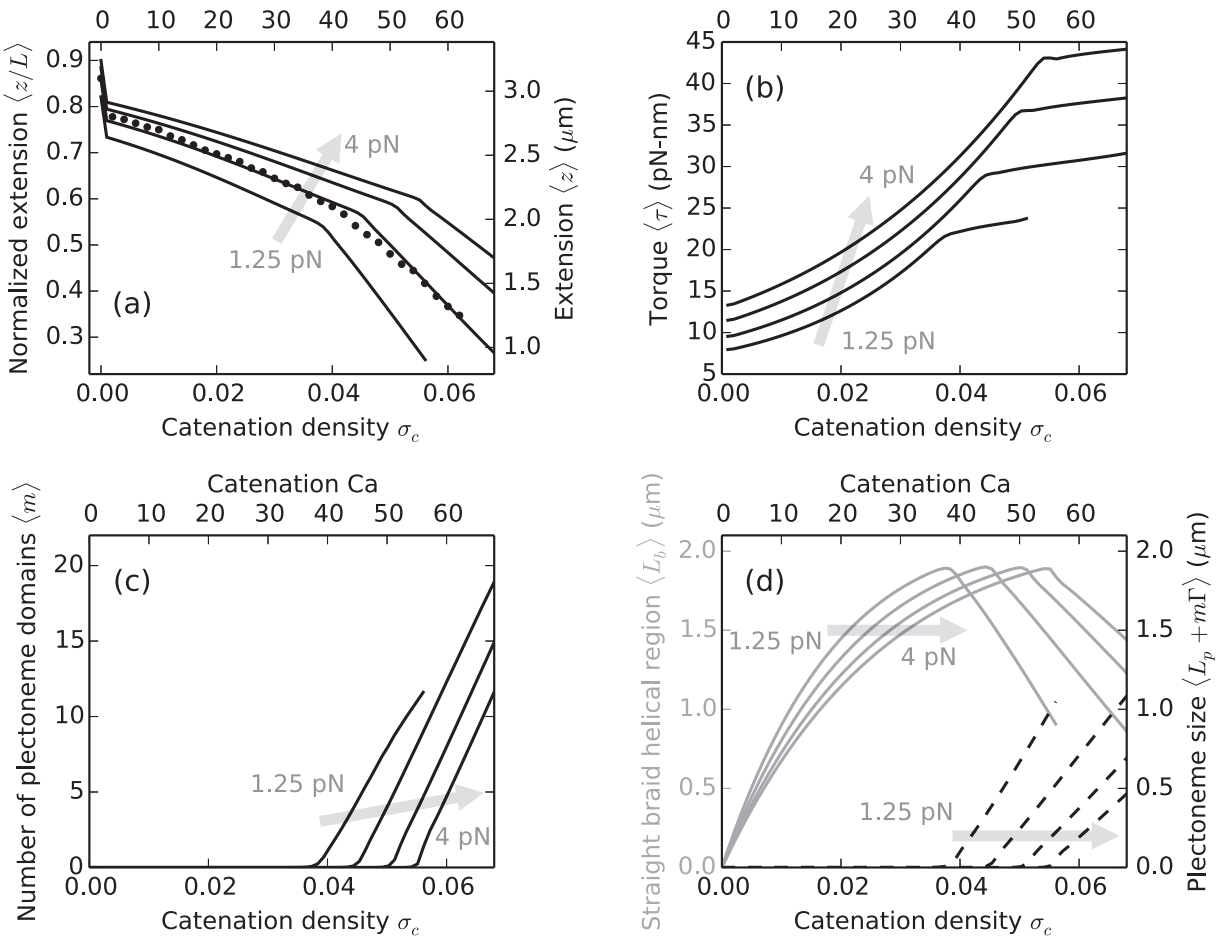

Figure 2.1: Analytical properties of the system, via [14].

These energies depend principally on structural parameters, among which R_p, P_p, $\mathcal{R}_p$, $\mathcal{P}_p$, that are respectively the radius and the pitch of the straight braid and the plectonemic braid, are the most important. Given this characterization it is possible to study the system free energy as a function of the catenation number (Ca) taken as the linking number (see appendix B) between the strands, and the pulling force applied to the upper extremities (f).

$$F(L_p, m) = min_{Ca_s}(\mathcal{E}_s(f) + \Delta\mathcal{F}_s(f) + \mathcal{E}(f) + \Delta\mathcal{F}_p)$$

The total free energy of the braid for each fixed plectoneme length (L_p) and number of plectoneme can be obtained through minimization over the catenation of the straight phase Ca_s. Along with this operation it is possible to thermally average over the values of L_p and m to obtain a final expression for the system partition function $\mathcal{Z}(Ca, f)$, by constraining the total catenation $Ca = Ca_s + Ca_p$ and the total DNA length $L = L_s + L_p + \Gamma$, with $\Gamma = \sqrt{\frac{2\epsilon A}{\beta f}}$.

$$\mathcal{Z}(Ca, f) = e^{-\beta F(0,0)} + \sum_{m=1,2,\ldots} \sum_{L_p=\Delta}^{L-d} e^{-\beta F(L_p,m)}$$

The two terms in particular corresponds to the straight phase and to the sum over all possible coexistence states. Through the partition function it is possible so to evaluate the average extension of the system, $\langle \frac{z}{L} \rangle$, along with the torque $\langle \tau \rangle$, the number of plectonemese $\langle m \rangle$ and the length of the straight braid helical region $\langle L_b \rangle$. Once calculated it is possible to study such properties, as it represented in figure 2.1 with different values of the tension f. As it can be noticed, these characteristics depend on many factors, including the salt density of the solvent, while having a main dependence on the

catenation number (or catenation density) and on the pulling force. Different conditions corresponds to different results, and directly affect the plectoneme formation.

2.2 Magnetic tweezers

These theoretical results can be compared to experimental tests in order to prove the results' accuracy. Single-molecule magnetic tweezers have proven to be an ideal apparatus to study DNA mechanics, as they can twist and apply a stretching force to individual DNA molecules or to multiple strands. These apparatuses were pioneered by the invention of optical tweezers, which manipulate dielectric microscopic objects with the help of a focused light beam [23]. Magnetic tweezers were soon introduced after these early implementations to allow the manipulation of paramagnetic beads using a gradient of magnetic field. This method allows also to accommodate multiple DNAs, with the possibility to stretch and twist the macromolecules.

The apparatus consists mainly in a flow cell where the molecule is tethered between a glass surface and a paramagnetic bead through non-covalent bonds resisting to forces up to 100 pN, while the other extremity is fixed to a non-moving bead [24]. The pulling force is exerted by a magnetic field applied over the bead, which has its own magnetic moment, and can be changed by moving the permanent magnets either up or down. This force is experimentally determined through the computation of brownian motion along one of the main axes. Twisting can instead be introduced through the rotation of the magnets, allowing to introduce supercoiling and plectoneme formation in the experimental setting.

Such experimental apparatus also needs a computer program able to track the bead in 3D space and report the position in real time, along with the presence of a second bead used as a reference to compensate for the instrumental drift. The beads positioning and the macromolecule's properties such as the extension can be measured through the analysis of diffraction images using incident light with wavelength comparable with the bead size.

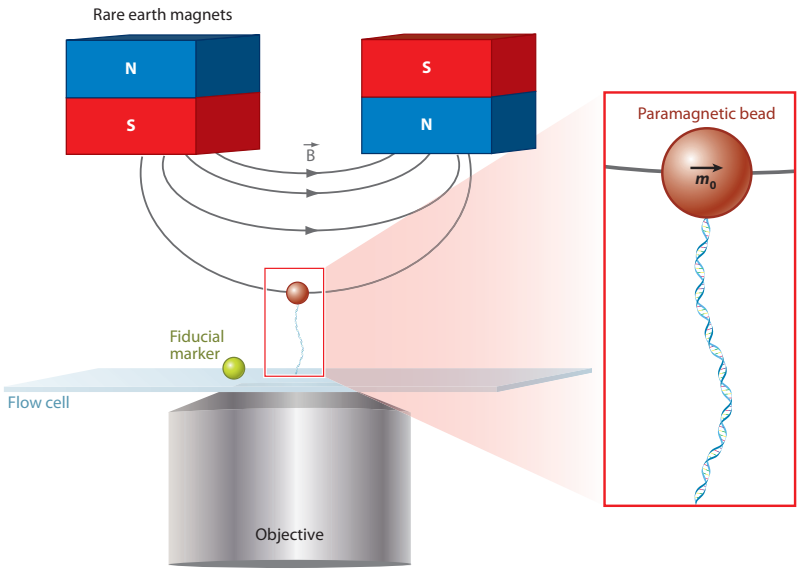

Figure 2.2: Magnetic Tweezer apparatus example, via [25].

The joint use of magnetic tweezers and fluorescently label DNA molecules [8] allows improving the static imagery obtained through the electron and force microscopy, showing that supercoiled DNA is plectonemic without giving any information on the dynamics. The combined use of these two techniques allowed getting an almost complete visualization of plectoneme behavior in force constrained systems, along with structural measurements of the DNA strands themselves.

2.3 Simulations of 2-strands environments

Since experimental results are difficult to be obtained, a more interesting approach is to try simulating the studied environments through molecular dynamics. In previous works [17] the use of LAMMPS allowed to study and reproduce the behavior of two braided strands. The interest of such works is to reproduce the experimental conditions of magnetic tweezers by fixing the extremities of the strands to elements representing the beads and the lower walls. DNA is simplified by introducing a coarse-grained [10] model of DNA through the use of a string of discrete beads emulating the behavior of the global dsDNA macromolecule. The magnetic tweezer's bead is instead replaced with a rigid "wall" of molecules moving together, to which the simulated braid is bonded. The other extremities are instead fixed to the bottom of the simulation box.

As for magnetic tweezers, it is possible to measure the main features of such braided systems, as for example the total extension or the single-strand writhe (see appendix B). With more advanced methods is also possible to correctly detect plectonemes and study their statistics and dynamics.

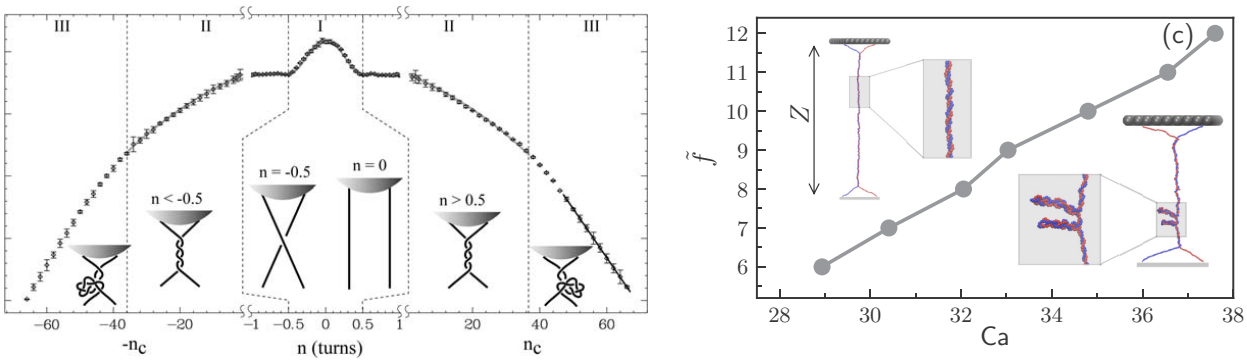

Figure 2.3: Plectoneme formation dependence on catenation via [12] (a), phase diagram, via [17] (b).

One of the main interesting points to analyze is the phase transition between the so-called "buckling" and "braided" phases. This kind of transition usually corresponds to the critical set of catenation number and force needed to allow plectoneme formation, and it usually corresponds to a change in slope of the braid extension plot vs force, as the formation of non-braided structures contributes to the reduction of the vertical elongation of the system. In figure 2.3 one can see how the phase transition is defined by a set of points, possibly joined by a transition line, through which it is possible to move from the braided structure to a buckled one presenting plectonemes.

It is possible with advanced methods to study also the dynamics of plectonemes, observing non-trivial phenomenons such as jumping and merging. These can be represented in Kymograph (figure 2.4), to represent the behavior of plectonemic structure.

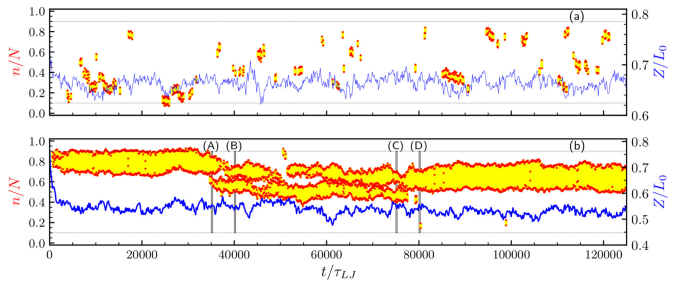

Figure 2.4: Kymograph, via [17].

A deeper insight of this topic can also include cases in which there is a kink in one of the chains, giving a complete different dynamics. In this work such topics will not be discussed, as the main focus will be on the influence of braid geometry on both the plectoneme dynamics and the phase transition displacement.

Chapter 3

Simulation settings and configurations

With the premises already done for the standard case (2 strands), it is possible to start discussing more and more complex environments. Given the increased interest in understanding the conditions and the behavior of DNA and chromatin [26], and on the form of structures generated by the braiding of multiple strands [20] it was decided to explore three-strands configurations, to understand if and how the theoretical and analytical results already found for the simpler cases could explain the behavior of the new system, and to discuss how different braid geometries influence the properties of the phase diagram. To characterize such phenomenons the first step was to introduce computational simulations in which an additional strand joins the standard two. Starting from previous approaches [17] the same LAMMPS configuration was instantiated with the additional potentials and settings necessary to simulate a three-strands system.

3.1 Polymer model

The polymer model considered during coarse-graining of the dsDNA structure is the standard worm-like model, where each bead of the strand is linked to the following one and the previous one through a harmonic potential, with the aim of representing the covalent bonds as ideal springs [18]. In this model, such interactions will be coded using potential both for two body interactions (single beads), and three body interactions (sequence of bonded beads).

For non-consecutive beads with spatial distance r the potential used is a Lennard-Jones one, with a fixed cutoff $r_c = \sqrt[6]{\sigma} + \Delta$ [17].

$$E = 4\epsilon_p \left[\left(\frac{\sigma_p}{r - \Delta} \right)^{12} - \left(\frac{\sigma_p}{r - \Delta} \right)^{6} \right] \qquad r < r_c + \Delta$$

For consecutive beads instead, the potential used is FENE [27] + LJ:

$$E = \underbrace{-0.5 K_e R_0^2 \ln \left[1 - \left(\frac{(r - \Delta)}{R_0} \right)^2 \right]}_{FENE} + \underbrace{4\epsilon_p \left[\left(\frac{\sigma_p}{(r - \Delta)} \right)^{12} - \left(\frac{\sigma_p}{(r - \Delta)} \right)^{6} \right]}_{LJ} + \epsilon_p,$$

where, beside the Lennard-Jones parameters σ, Δ and ϵ, the dependence is on R_0 and K_e, respectively the maximum extension of the bond and its strength. This summation is necessary for the potential to be both repulsive (LJ), and attractive (FENE).

The three-body interaction instead emerges when considering groups of three beads each. In particular, given the angle θ formed by three consecutive beads, the potential is given by the following equation:

$$E = K[1 + \cos(\theta)],$$

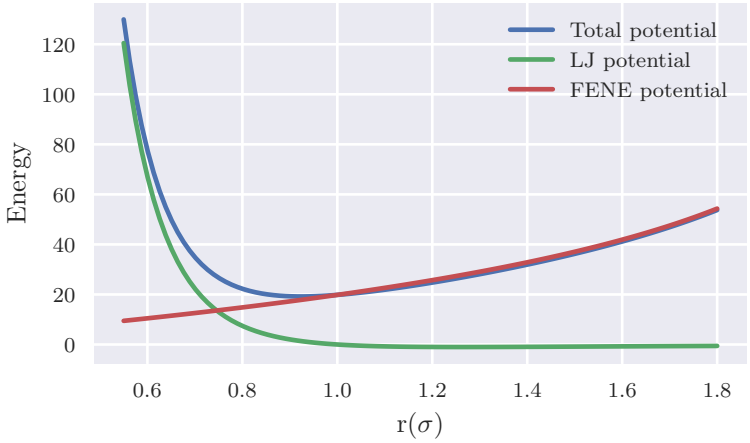

Figure 3.1: Comparison of the three potentials.

where K depends on the persistence length of the worm-like chain, and so is set accordingly. In the discussed case the persistence length is estimated to be 50 nm [17] and K assumes such value once rescaled according to the conventions (see next section).

3.2 Setting parameters

Each parameter is measured according to the Lennard-Jones units, which rescale the standard units according to the σ,Δ,ϵ parameters of the Lennard Jones potential. Energy is so rescaled as $E^* = \frac{E}{\epsilon}$, while distance becomes $x^* = \frac{x}{\sigma}$ and force is $F^* = F\frac{\sigma}{\epsilon}$.

The σ parameter depends on the simulated system, and in this configuration it corresponds to the diameter of double-helix DNA, estimated to be around 2.5 nm. The ϵ parameter can be calculated instead as $\epsilon = K_bT$, where T is the system temperature, fixed at 300 K, giving so $\epsilon = 4.14 \cdot 10^{-21} J$. The mass in this system is a unitless ratio with a reference mass, that in the simulations is considered to be the mass of the beads composing the chain, while the beads of the moving "wall" have a mass fixed at 0.001. Finally, the time is scaled to the typical time of the system τ, the one needed for a bead to cover a diffusion length of σ. This can be calculated using the formula $\sigma^2 = 2D\tau$, where $D = \frac{K_bT}{f\eta}$,η is the viscosity of the water, $\eta = 1\frac{mP}{s}$ and f a geometrical factor, that, for the spherical beads, can be calculated as $f = \frac{3\pi}{2}\frac{\sigma^3\eta}{K_bT}$, giving $\tau = 17.8ns$.

Using this particular rescaling it is possible to fix the potential parameters, $\sigma_p = \frac{\sigma}{\sigma} = 1$, $\epsilon_p = \frac{\epsilon}{\epsilon} = 1$, $\Delta = 0$ for strings' beads, while for the wall's beads Δ has an higher value to take into account a larger bead diameter. For the bond potential, parameters are fixed to $R_0 = 1.5$, $K_e = 30$, while for the angle it was decided to assign $K = \frac{50}{\sigma} \approx 20.6$. The timestep is instead fixed at $t = 0.0025\tau \approx 0.0445ns$.

3.3 Dynamics

The dynamics of the system can be considered fully only by taking into account different phenomenons. The main interest of the discussed simulations is to reproduce the behavior of the strands through the coarse-graining and the beads' movement. The integration of the Langevin equation allows to obtain a temporal expression for such quantities.

$$m\frac{d^2\vec{r}_i}{d^2t} = -\nabla U_i \underbrace{-\lambda\frac{d\vec{r}_i}{\partial t}}_{\text{viscous force}} + \underbrace{\vec{\eta}(t)}_{\text{stochastic force}} ,$$

where U_i is the total potential on the bead i. In the equation both the natural viscosity of the fluid the strands are solved in, and stochastic force accounting for the collisions with the fluid particles are

taken into account and iterated to reproduce the braid displacement. The interaction between the strands and the lower wall is instead implemented through a harmonic repulsive potential, reproducing the effect of a spring with a high elastic constant.

$$E = \epsilon(r - r_c)^2 \quad \epsilon = 200, r_c = 1$$

The forces used in the tested cases are applied to a single bead, placed in the center of the upper rigid "wall", allowing to pull the braid with a chosen strength. Rotations are instead implemented directly on such wall and influence directly the braid, introducing non-zero linking numbers.

3.4 Simulation environment

The environment considered during the simulations is not very different from the already discussed two-chain case. The strands were chosen to be composed of 250 beads with diameter fixed to σ, while the upper wall size was adapted to the different discussed geometries. To improve the knowledge on such multi-stranded chains it is in fact necessary to test different configuration, by changing the chains' displacement on the two anchoring xz planes, while y becomes the axis on which the braid is vertically distributed.

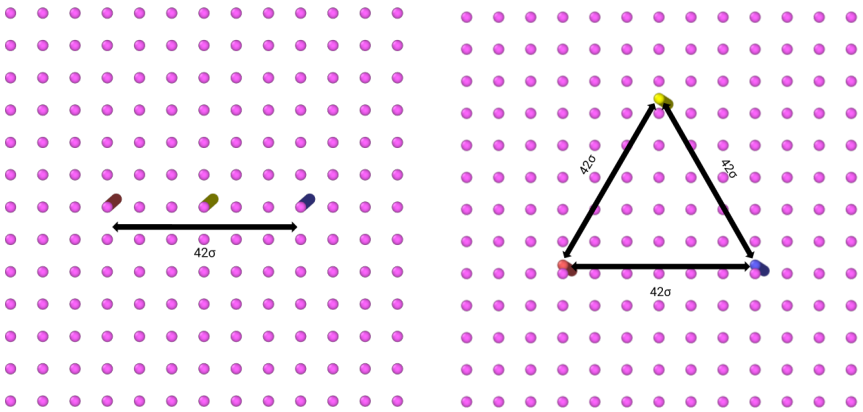

Figure 3.2: Wall and beads positioning, with distance between red and blue strands anchoring points fixed at 42σ.

It was decided to braid both aligned and "triangular" fashions of braids, as it can be seen from figure 3.2, while changing the relative distance of the strands' extremities. This allowed both to explore the effects of the simple addition of a chain beneath the other two, and to verify the outcomes of the presence of a "disturbing" strand misaligned with the original configuration. From now on, when discussing the results, the configurations with three chains will be referred as 3-strands, while the one with two chains will be referred as 2-strands.

Chapter 4

Aligned strands

A first approach to new configurations with three strands was to place a third strand in between the original two. This new chain maintains the properties of the original ones while constituting an obstacle during the braiding process, being in the middle of the other two strands. The stress related to the third strand getting stuck in between the other two allows the system to reach different conformations and influence the phase transition process. Four different configurations were prepared in order to

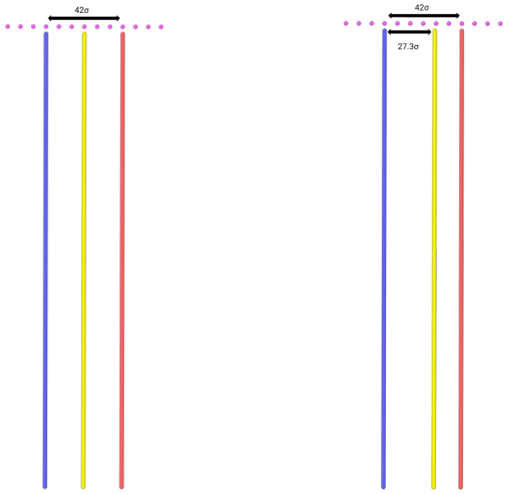

(a) (b)

Figure 4.1: Aligned configuration with distance between red and blue strands anchoring points fixed at 42σ, in (a) the third strand (yellow) is placed exactly in the middle, while in (b) it is placed at the 65% of the distance between the main strands.

appreciate different features of the newly discussed configuration, in particular by considering different relative distances between the external strands. This value was fixed alternatively to 6σ and 42σ in order to compare new results to the old ones. For what concerns the geometry the newly generated strand was placed in the middle of the other two, or at the 65% of the segment joining the external chains' extremities, as shown in figure 4.1.

Such configurations are then taken and rotated by applying a large force (40 pN, or eventually more) to keep the braid configuration as much as extended as possible while the rotation was rigidly applied to the upper wall. The final configuration is different for each chosen catenation number (in this case representing both the number of rotations and the linking number between pairs of strands). The final analysis was then done on the equilibrated configuration obtained while pulling the braid with different forces.

As seen in chapter 1 the braided phase is analytically modelled as a double helix with an average pitch and radius. With three strands the system is more and more complex, but the helicoidal structure

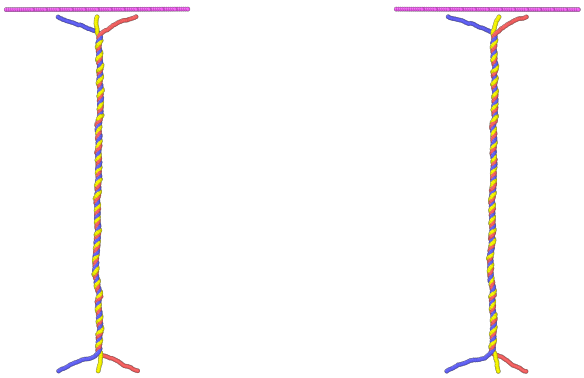

(a) (b)

Figure 4.2: Braided aligned configuration (Ca=26, F=28.35 pN) with distance between red and blue strands anchoring points fixed to 42σ. In (a) the third strand is placed in the middle, in (b) is placed at 65% of the segment.

seems to be conserved as it can be noticed in figure 4.2. Tests were also done to check if results obtained for positive catenation number were identical to the ones obtained for negative catenation number (anticlockwise rotations). This has proven to be true for all the tested cases (even the ones with shifted third strand), for which all the main features were identical (e.g. extension, plectoneme number and total length) or opposite (e.g. single strand writhe).

4.1 Distance 6σ between anchoring points

4.1.1 Main features

A first analysis is based on the extension vs force curves, calculated as the ratio between the average extension during equilibrium simulation of the three chains and their maximum extension possible (250σ). It is possible to verify that the appearance of non-braided structures is deeply linked with a change in the trend in the extension plot, since the structure moves from a helix-like configuration to a "buckled" one in correspondence to the transition. To get an estimated extension, the final value for each tested configuration was obtained by averaging over the considered strands and the total time the simulation was run. In order to get the least biased possible average and standard deviation,

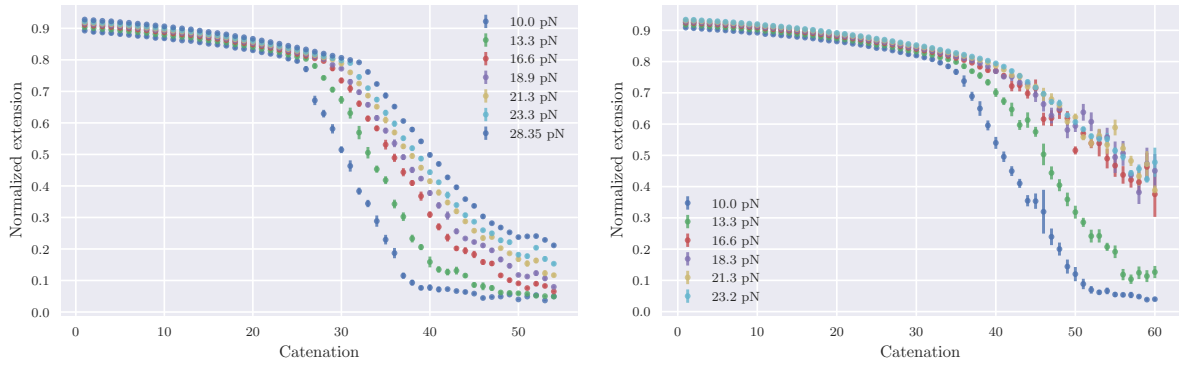

(a) (b)

Figure 4.3: Time and strand-average end-to-end vertical distance for the aligned case with base length 6σ(a), and the 2-chains case with distance 6σ(b).

the samples taken into account were selected according to the integrated autocorrelation time [28], by sampling a subset of values in order to get the least possible autocorrelation. In addition to this the computation was done only when the braid was fully equilibrated, by excluding the first 5000000 steps. It can be noticed how the change in the number of strands affects a lot the average extension,

mainly in the shape of the line, while, as expected, the buckling transition seems to be present also for these configurations with a sudden change in slope. In this case the transition positioning is much different from what can be seen in the 2-strands case, with a shift in catenation number of almost 10 as it can be observed in figure 4.3.

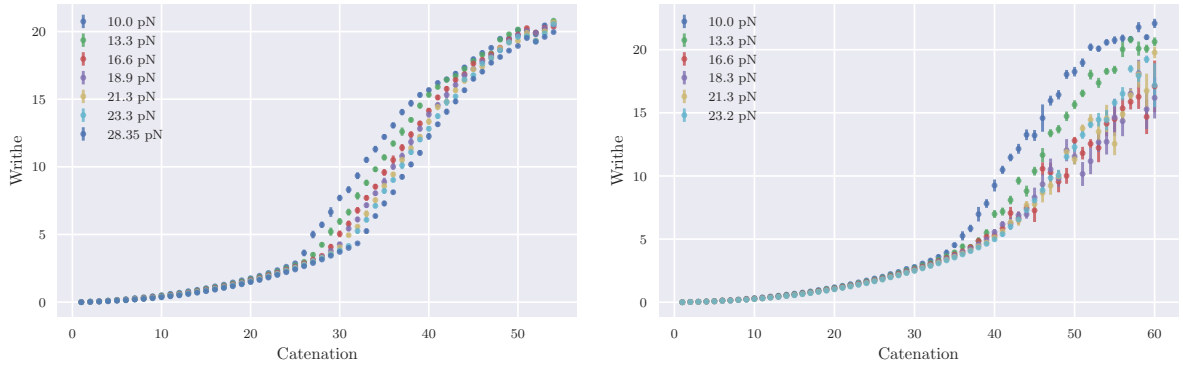

(a) (b)

Figure 4.4: Time-average single-strand writhe for the aligned case with base length 6σ(a), and the 2-chains case with intertheter distance 6σ.

The single strand writhe in figure 4.4 can also be calculated and compared to the two chains case. It can be noticed how the transition between buckled and unbuckled phase is clearly marked with a change of slope and the behavior is pretty much the same, beside the translation due to change in geometry of the system. This is in general associated to the transformation of local twist in writhe inside non-braided structures, increasing the total writhe value. These results come from a single strand, the first one, since for all the analyzed chains the total writhe was almost equal. The final value was also calculated according the integrated autocorrelation time in order to improve the computation reliability.

4.1.2 Phase diagram and phase transition

The phase diagram transition points were obtained by fitting with a double curve the extension vs force plot. In particular a straight line was used to fit the right part of the diagram, while a parabolic curve was instead used in the left part in order to adapt to the two trends presents in such diagrams. Points were selected arbitrarily in order to obtain the best accuracy for the double fit and the transition point identification. Two cuts were made for each fitted diagram, one horizontally, to divide the buckled and unbuckled zones, and a second one vertically, to avoid fitting on regions where the graph was no more approximable with a parabolic or linear behavior respectively. The intersection between these two lines was then calculated and used as a reference for the phase diagram definition. The fit precision is usually very far from perfection, especially for the two chains case, but can give a very reliable estimation of the transition points displacement for the different discussed cases along with the error associated to the intersection accuracy.

From the phase diagram in figure 4.6 it is possible to observe the already discussed effects of the change in geometry on the phase transition displacement, with a massive shift in the critical catenation at fixed force. This effect can be partially explained by force rescaling if the three chains are thought to be simple springs, with the global elastic coefficient expected to be $\frac{3}{2}$ of corresponding one measured for two strands. In parallel the shift in catenation is on the other hand more difficult to rationalize and may be associated to the deep implications of the helix geometry change in the three chains case.

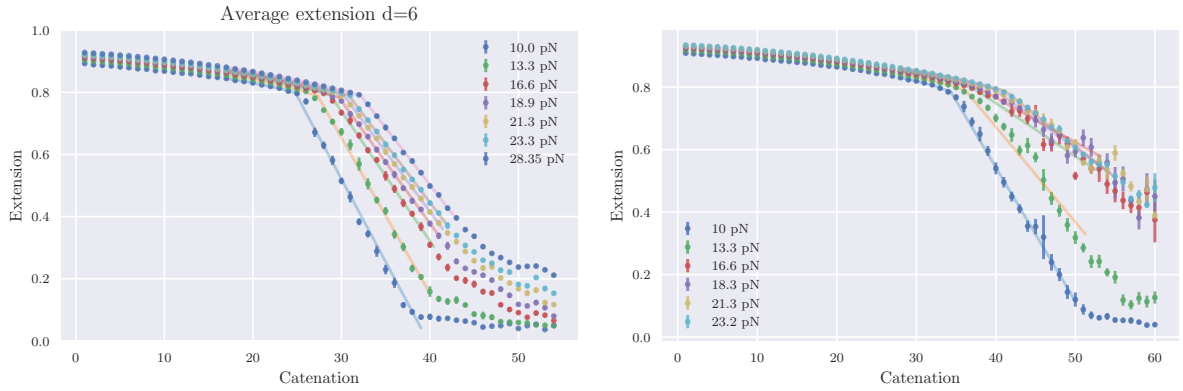

(a) (b)

Figure 4.5: Time and strand-average end-to-end vertical distance for the aligned case with base length 6σ(a), and the 2-chains case with intertheter distance 6σ(b). The superposed lines represent the two fits' result.

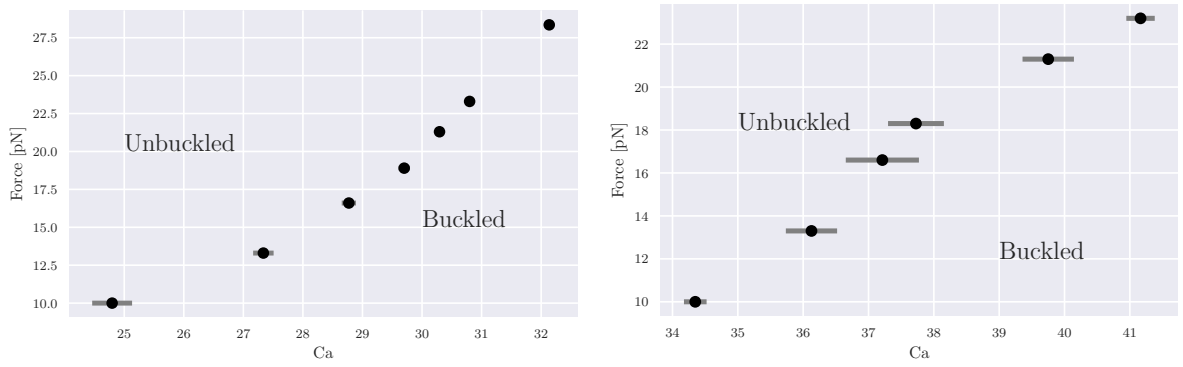

(a) (b)

Figure 4.6: Phase transition diagram for the aligned case with base length 6σ(a), and the 2-chains case with intertheter distance 6σ(b).

4.1.3 Plectoneme statistics

Plectoneme appearance has a whole different set of problems for detection. In fact, it is in general difficult to detect the presence of a plectoneme without looking by eye at the simulated configuration. To avoid this necessity numerous techniques were tested, from the use of contact maps [17] to the exploitation of local writhe [29]. The first approach consists in analyzing the relative distance of each pairs of beads and verify if any combination that would be very distant in a normal configuration (with straight strands) is closer than a fixed threshold. Eventual anomalies can be directly associated with the presence of non-straight braids and plectonemes formation. This method allows to detect both visually and computationally the alleged plectonemes that were found in the simulated strands, and it works optimally in the 2-strands case.

The contact map in figure 4.7 shows the presence of plectonemes through eyesight. This approach can be also coded using algorithms to translate the method in a more functional way, by checking automatically the distance between beads. A plectoneme is in fact detected if the distance between the selected beads is smaller than a chosen value and the index difference is higher than another fixed threshold.

The different used thresholds are associated to the different configurations considered during the analysis. These thresholds are calculated by approximating the minimum possible loop that can be generated as a circle with radius dependent on the kind of configuration. In figure 4.8 two examples of the minimum possible configurations are shown with their relative threshold parameters. For the 2-strands case this radius can be in fact approximated to 2σ, while for three strands is 3σ, giving

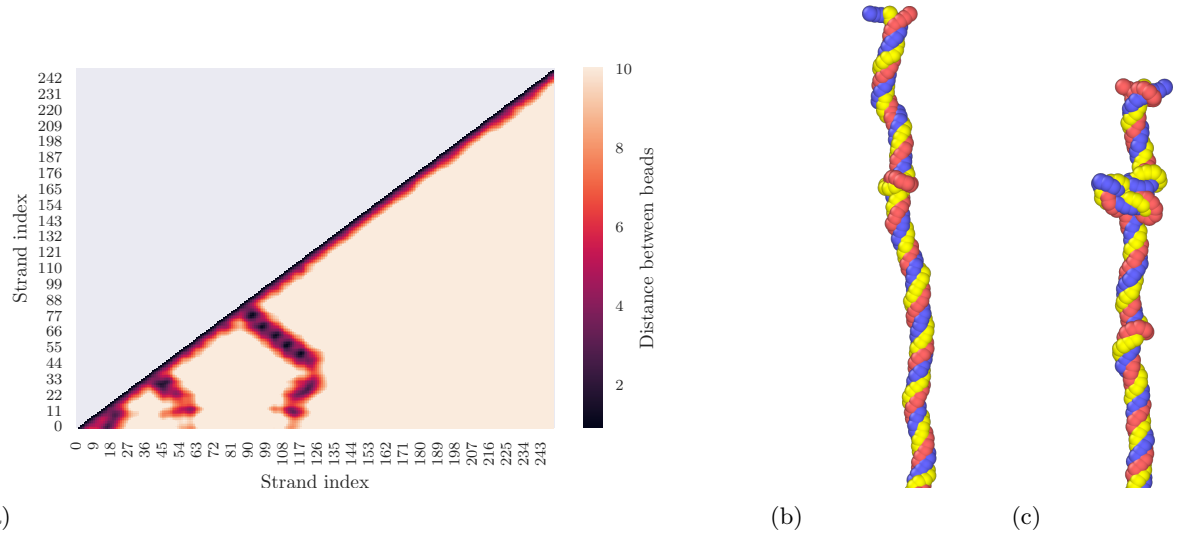

Figure 4.7: Contact map in a three strands case with distance threshold 10σ. The image refers to a step in the simulation with force fixed at 10 pN and catenation fixed at 31 (a). Non plectonemic(b) and quasi-plectonemic(c) structure formation in linearly aligned configurations at pulling force fixed to 16.6 pN with catenation respectively 30 (b) and 31 (c).

the threshold of respectively 13σ and 18σ, obtained through the multiplication by 2π. The distance threshold is instead fixed at 3σ for both cases. After having detected the alleged plectonemes for each chain, if their position is superimposed they are merged by taking the average of detected begin and end indexes. This is done for each chain, with the final position and number of plectonemes obtained from the chain with the least plectonemes, to avoid overestimation of both total length and number.

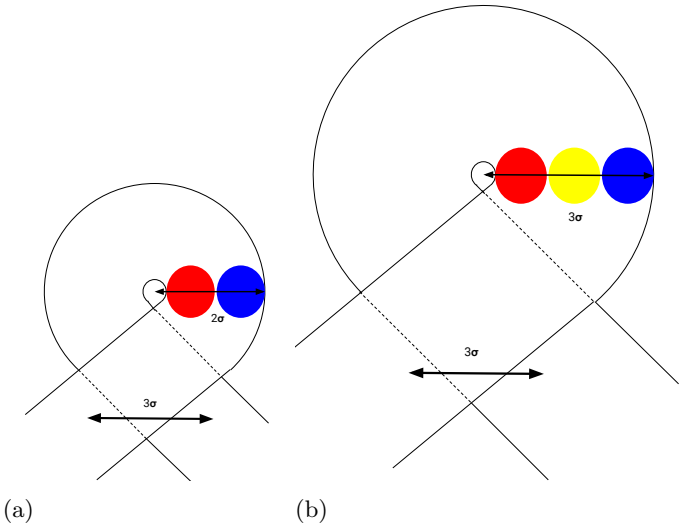

Figure 4.8: Thresholds used for the two different discussed cases.

This method has proven to be working well in the case of two strands, where almost all the plectonemes were correctly detected, except for some cases in which non-plectonemic (e.g "solenoids") structures were confused as plectonemic ones. The detection problem become very relevant when discussing configurations with three chains, in which "solenoidal" [11] configurations become prevalent in the braid after the buckling transition has taken place.

As it can be seen from figure 4.7, solenoidal structures are not strictly plectonemes but some sort of

intermediate configuration between the straight braid and a plectonemic one, representing sometimes nucleation point of plectonemic structures. Despite this structural difference they contribute to the change in extension and in writhe with continuity with the standard plectonemic phase and so cannot be separated in the phase diagram directly from it. During the detection they can be easily confused with plectonemes and so, to avoid recognition problems associated to these kinds of structure, there was in fact the necessity to introduce a new method to discriminate the false positives identified as plectonemes with the original technique. Starting from the alleged list of plectonemes positions, it is possible to calculate the local writhe of the single strands to find peaks possibly corresponding to plectonemes [29]. This allows to exclude non-plectonemic structures that instead do not present a local peak in writhe.

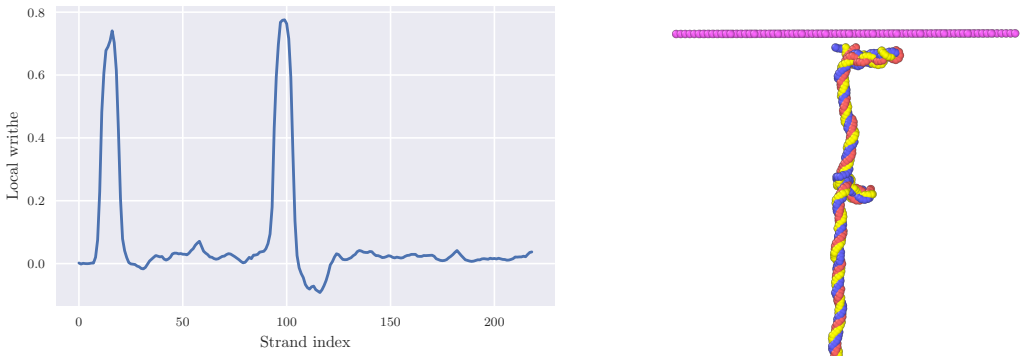

(a) (b)

Figure 4.9: Local writhe for the case with force fixed at 10 pN and catenation 30 for a three chains configuration (a). Corresponding braid configuration (b).

As it can be noticed from figure 4.9 the presence of plectonemes is clearly visible and distinguishable from both solenoidal and braid phases with lower local writhes. The computation was then exploited within a window of 16 position, and the cut on the peaks fixed at 0.5. Only detected plectonemes satisfying these prerequisites were actually taken into account during the analysis.

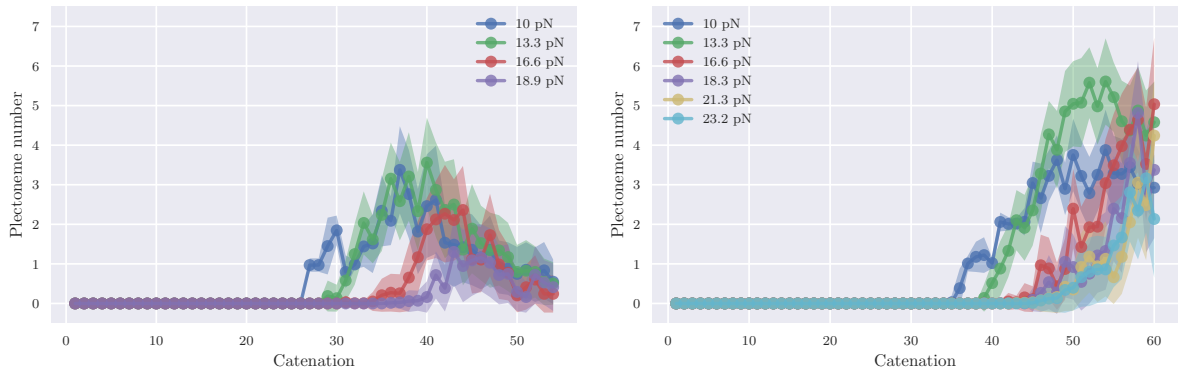

(a) (b)

Figure 4.10: Time-average detected number of plectonemes for the aligned case with base length 6σ(a), and the 2-chains case with intertheter distance 6σ(b).

As it is possible to notice from figure 4.10 plectoneme appearance follows for low catenation numbers and small forces a trend similar to what seen for the two chain case, shifted according to the new phase transition rule, while the global behavior is instead very different. It can be seen that for very large forces plectonemes are not even present, leaving room mainly to solenoidal structures, while for large catenation numbers the braid forms a very disordered configuration reducing to a very small globular structure, that will be discussed later in chapter 6.

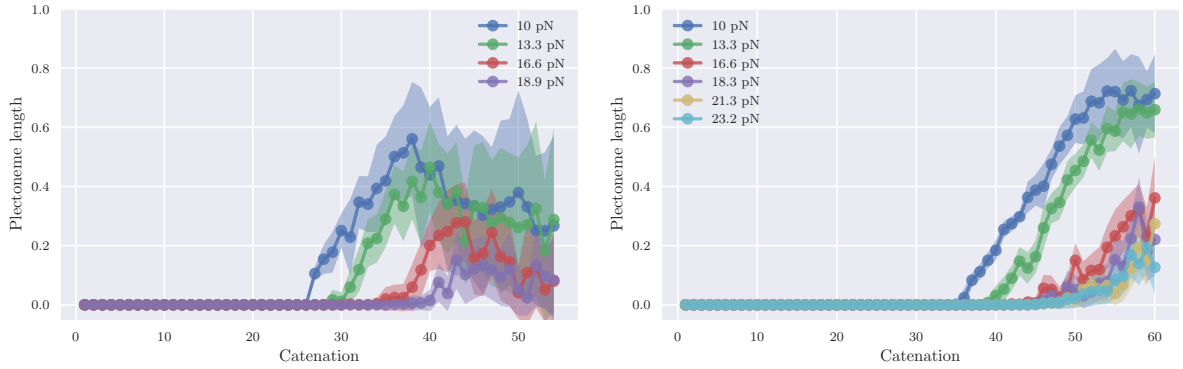

(a) (b)

Figure 4.11: Time-average cumulative plectoneme length for the aligned case with base length 6σ(a), and the 2-chains case with intertheter distance 6σ(b).

The length trends in figure 4.11 are also similar to what was seen in the two chains case, with the simulations run at smaller forces giving larger total normalized length. The total length begins to decrease as before, when the catenation number is too large, with the estimation becoming very noisy due to the small number of detected plectonemes.

Globally the most reliable analysis can be done only up to a certain catenation number (≈ 40 in this case), beyond which the conformations are too compressed, and it becomes very hard to drive any conclusion.

4.2 Distance 6σ between anchoring points, third strand shifted

The second configuration that was taken into account consisted in a three-strands geometry with the additional chain shifted toward the red chain in representations. This kind of configuration was produced in order to check if the geometry of such systems has any symmetry dependence on the position of the chain. Graphically it was possible to notice in simulations that the main difference in the introduction of this change was related to the positioning of the braid, as it seemed more shifted towards the initial position of the third chain.

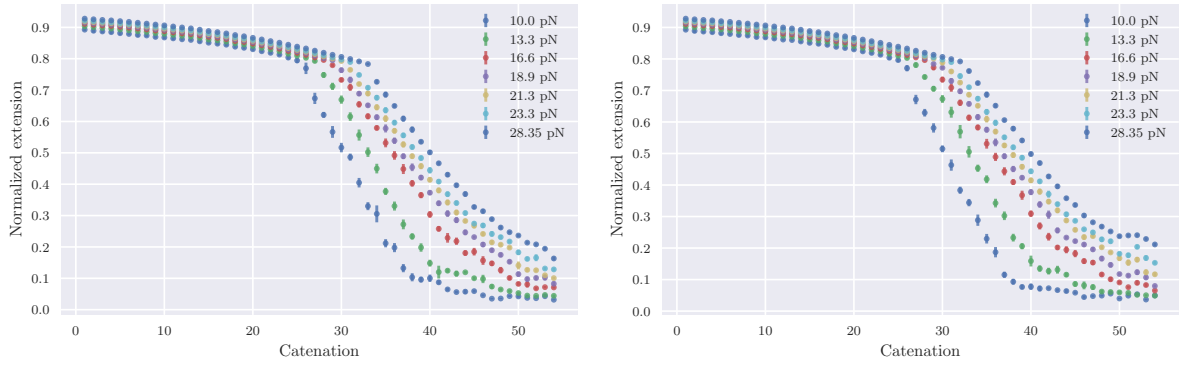

(a) (b)

Figure 4.12: Time and strand-average end-to-end vertical distance for the aligned and shifted case with base length 6σ(a) and for the aligned case with base length 6σ(b).

As it can be observed from figure 4.12 the main characteristics remained instead unchanged with the resulting extension behavior almost identical to what was seen in the previous case, with the absence of any significative change in both the values and the trends. This result is probably associated to the invariance in braid length between the two discussed cases, with the distance between the three

strands being not large enough to influence the phase diagram, as it can be also observed in figure 4.13.

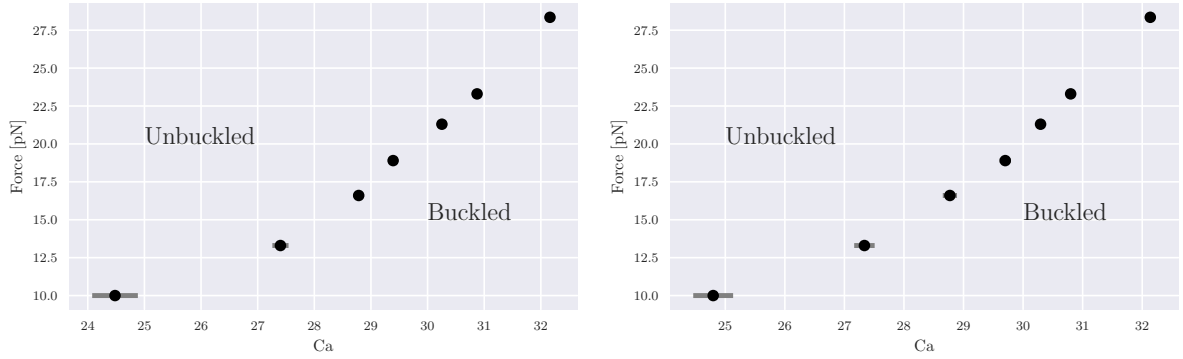

(a) (b)

Figure 4.13: Phase transition diagram for the aligned and shifted case with base length 6σ(a), and the aligned case with base length 6σ(b).

It is possible to conclude so that plectoneme and buckling statistics are not influenced by these change in geometry, at least for the configuration with distance between the external chains equal to 6σ.

4.3 Distance 42σ between anchoring points

To trigger possible new results it was decided to explore configurations involving larger distances between the "external" strands, trying to exploit new behaviors in phase transition and plectoneme dynamics. In this kind of configurations the displacement of the strands reduces the available length of the braid, since the initial and final parts of the chains are required to link the extremities to the braid ends, as it can be seen from figure 4.14.

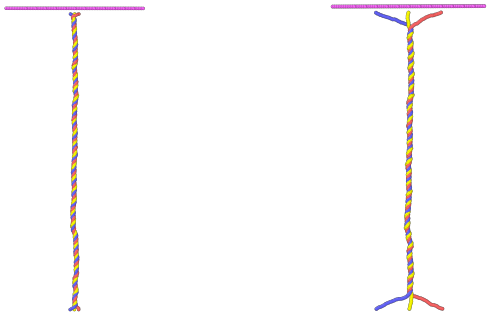

(a) (b)

Figure 4.14: Braided aligned configuration (Ca=26, F=28.35 pN) with different distances between anchoring points. In (a) the base length is 6σ, while in (b) is fixed to 42σ.

4.3.1 Main features

As expected from the new geometry the extension plot in figure 4.15 is much different from what seen in the case with smaller displacement distance(6σ), with a very noticeable shift to the left in the x-axis and a steeper slope in the first part of the graph. Instead, if it is compared to the old two-chains case the shift in catenation number is clear, and similar to the one already noticed in the previous sections.

Similar observations can be also done for the single-strand writhe in figure 4.16, with a shape similar both to the old two-chains case and to the ($d = 6\sigma$) case of the previous sections. The shape change associated to the buckling transition is present in the graph, while the points associated to the different tested forces seems to be tighter than what was seen in the previous chapters.

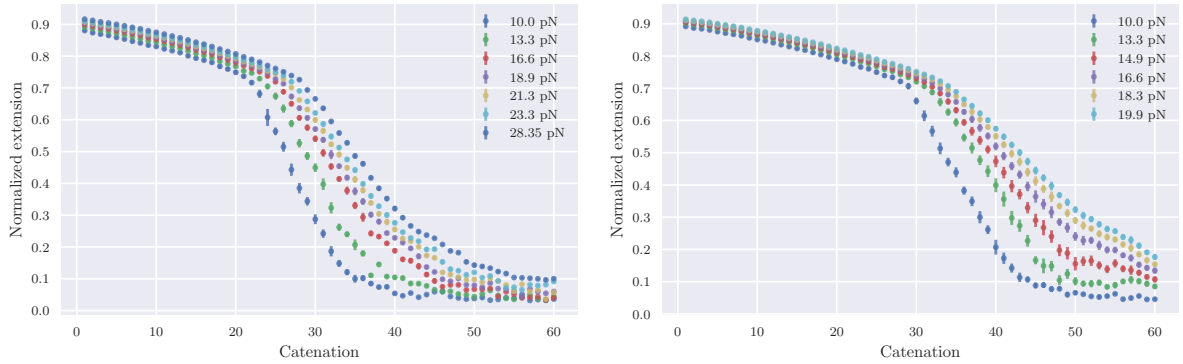

(a) (b)

Figure 4.15: Time and strand-average end-to-end vertical distance for the aligned case with base length 42σ(a), and the 2-chains case with intertheter distance 42σ(b).

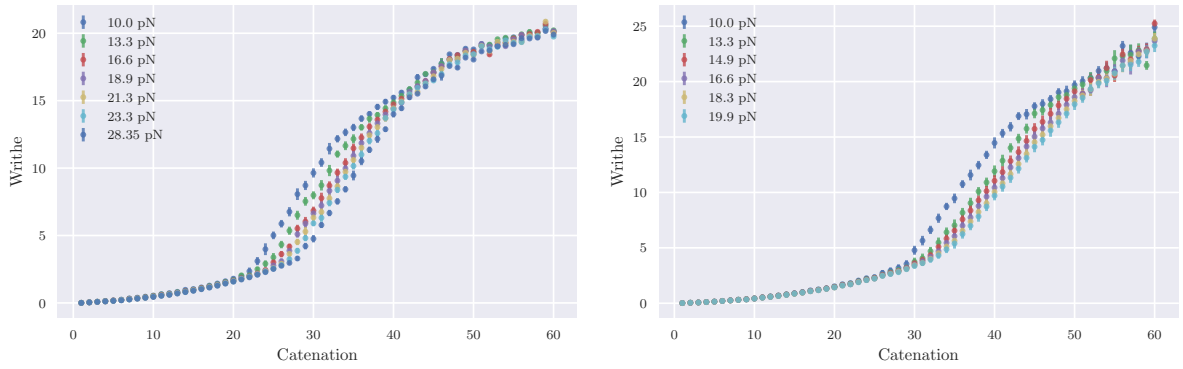

(a) (b)

Figure 4.16: Time-average single-strand writhe for the aligned case with base length 42σ(a), and the 2-chains case with intertheter distance 42σ.

4.3.2 Phase diagram and phase transition

As was done for the $d = 6\sigma$ configuration it is possible to analyze and discuss the plectoneme statistics if the geometry is widened. From what was already seen in the extension plot vs catenation discussion it can be concluded that the phase transition thresholds has changed with an additional shift in catenation number. This reflects in the plectoneme population, that resembles the one already seen in the previous sections, with a difference in the minimum catenation number required to develop plectonemes. Besides, the global behavior is mostly similar, with the already highlighted increase in number before a successive decrease visible in figure 4.17. If compared to the two-chains case the average number of plectonemes is much smaller, but it is possible to notice similar trends on the largest tested catenation numbers. The total plectoneme length in figure 4.11 offers a behavior similar to the average total number of plectonemes, with less accurate measurements probably associated to the noise. Again, the trends in the two-chains and three-chains cases are very different, with the same peculiarities already observed for the number of plectonemes, while the presence of some unexpected peaks in the high catenation zone are probably associated to the low statistics present for the analysis.

Finally, it is possible to discuss the transition plot obtained from the intersection of the two lines fitting the extension plot. The graph in figure 4.19 seems to highlight the additional shift that was present in both the extension plot and the plectoneme statics. The change in geometry has a large influence on the phase diagram, and is probably associated to the decrease in the length of the braid. Such change adds stress to the configuration and forces to express it through solenoidal or plectonemic formations. More tests were done using this configuration, including the movement of the middle chain along the axis linking the two main strands, to check if any dependence on symmetry could influence

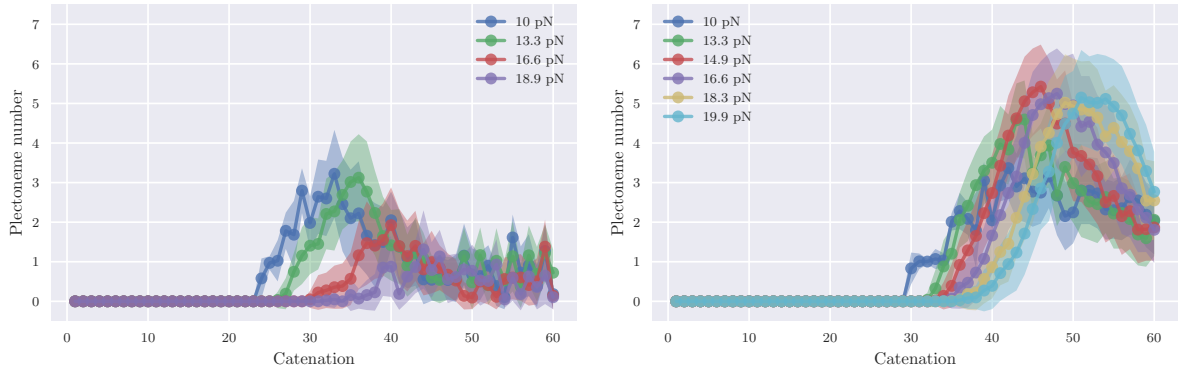

(a) (b)

Figure 4.17: Time-average detected number of plectonemes for the aligned case with base length 42σ(a), and the 2-chains case with intertheter distance 42σ(b).

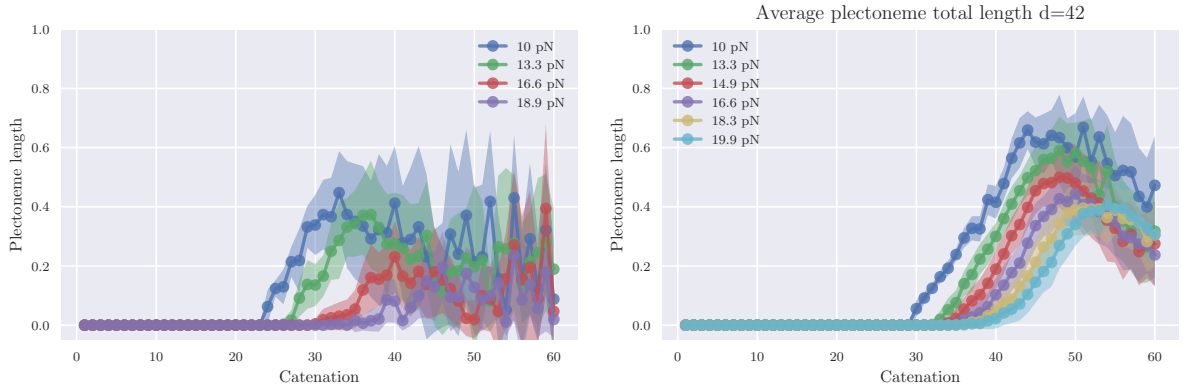

(a) (b)

Figure 4.18: Time-average cumulative plectoneme length for the aligned case with base length 42σ(a), and the 2-chains case with intertheter distance 42σ(b).

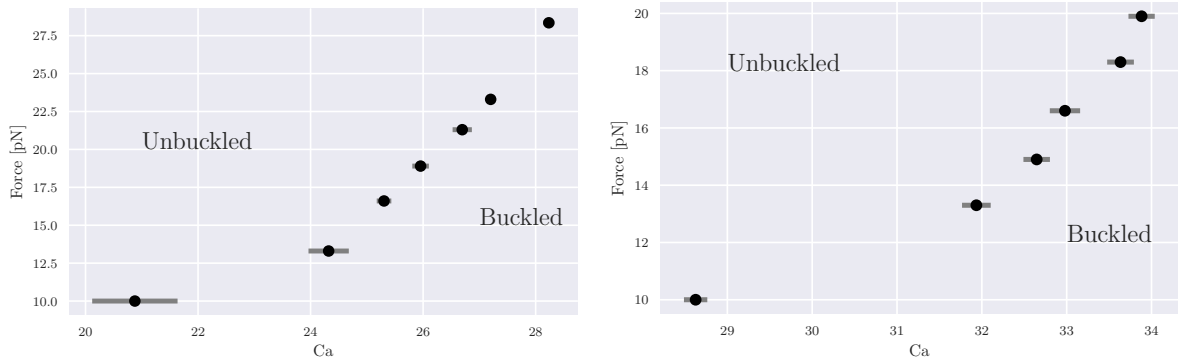

(a) (b)

Figure 4.19: Phase diagram for the aligned case with base length 42σ(a), and the corresponding two chains case 42σ(b).

the discussed results. None of them showed any valuable difference from the ones presented in this section, allowing to conclude once again that stronger effects can be only induced with a stronger change in geometry.

These results were already presented in a previous work for 2-strands cases [17], where this effect was linked directly to the change in the distance between the anchoring points of the chains. Similarly

to what was observed before, a geometric change (previously a distance increase between anchoring points, now the addition of a third chain) influences a lot the phase diagram, mainly by reducing the critical catenation number at fixed force. Such geometrical change affects also the way in which buckled structures are manifested, with the increase of solenoids population and the diminishing of plectonemic structures. In the next chapter it will be then discussed how the third chain anchoring point displacement allows too to change the system stress, triggering similar phase diagram variations.

Chapter 5

Triangular layout

This chapter will deal with more general configurations allowing a free displacement of the braids extremities in the xz plane, such that they will distribute as triangles with different side lengths. This approach was tried to study more in general the effect of the third chain once added to the two-chains configurations, without any constraint associated to the alignment of the strands.

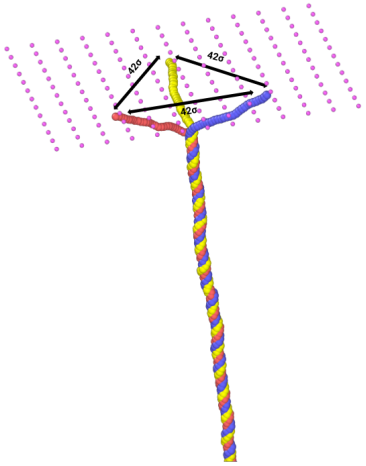

Figure 5.1: Braided triangular configurations with side length equal to 42σ at catenation number equal to 26 and applied force 28.35 pN. Image tilted for visualization necessities.

Cases tested concerned the same distances between external strands, with 6σ and 42σ lengths, which can be compared to the "aligned" cases discussed in chapter 4. The angles at the base of the considered triangles instead varied in the range between 15° and 80°, allowing to study different configurations of braids. All the tested configurations were isosceles, given that, as it will be seen later, the only parameter that affects the phase transition seems to be the distance between the newly added strand and the other two.

5.1 Equilateral configuration with base 6σ

As done in chapter 4 the first tested configuration involved a distance between the starting strands equal to 6σ. The choice of an equilateral triangle (60° base angles) was done to get the most balanced configuration possible, with the upside of a symmetrical displacement.

Repeating the analysis already done in chapter 4 it was possible to get some insights of the new behavior, along with a comparison to old results. In figure 5.3 are present side by side the average extension values in the aligned and triangular configuration. The resulting trends are practically identical between the different configurations, with both the values and the slope change distributed in the same exact way. This kind of behavior is repeated in the writhe plot in figure 5.4, showing again

(a) (b)

Figure 5.2: Braided equilateral triangle configuration (Ca=26, F=28.35 pN) with base length 6σ between red and blue strands anchoring points and aligned configuration. In (a) the strands form an equilateral triangle, while in (b) are linearly aligned. Image tilted for visualization necessities.

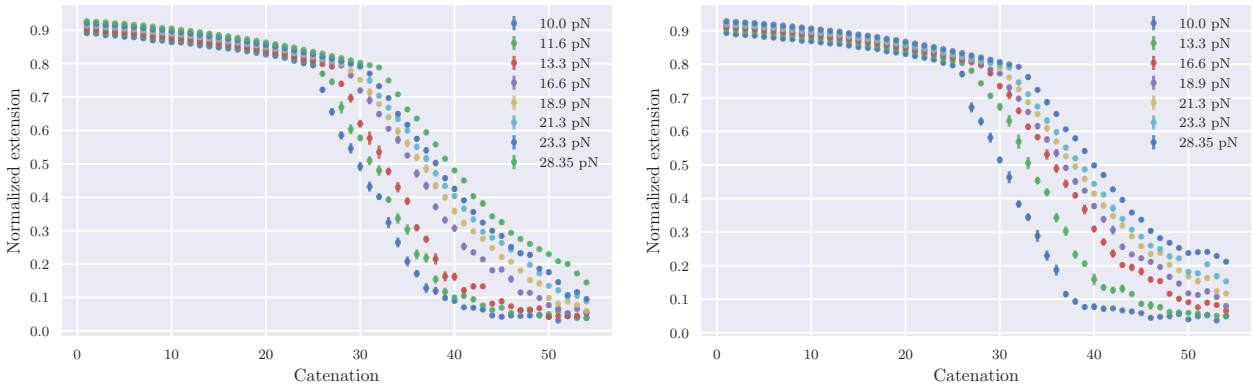

(a) (b)

Figure 5.3: Time and strand-average end-to-end vertical distance for the equilateral triangle configuration case with base length 6σ(a), for the aligned case with base distance 6σ(b).

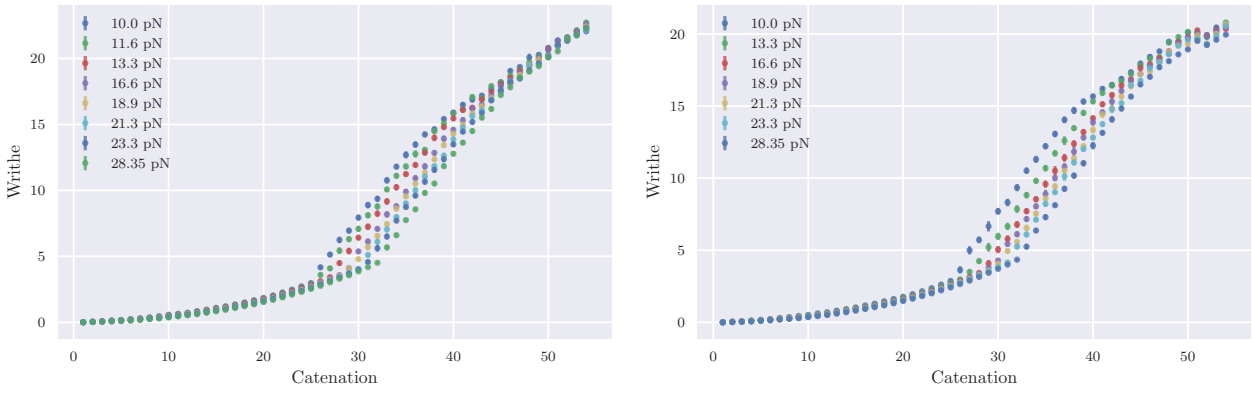

(a) (b)

Figure 5.4: Time-average single-strand writhe for equilater triangle with base length 6σ(a), for the aligned case with base distance 6σ(b).

the slope change expected and associated to a buckling transition distributing almost identically to the one for the aligned configuration. From these comparisons it seems possible to conclude that the braid buckles in the same exact way it did in previous configurations. The geometry may be a critical

factor in this result, since from the simulation representations (figure 5.2) it is possible to notice that the triple helix seems to have identical structure and feature if compared to the aligned one. The resulting identical behavior may be a direct consequence of this conformation.

A final comparison can be done using the phase diagram of figure 5.5. Given that the points were obtained in the same way for the two cases, the results are very similar if not almost identical, confirming once again the similarities between the two configurations. It is possible to conclude that the phase transition, even if limited to the buckled and non-buckled phases, is practically identical between the two geometries.

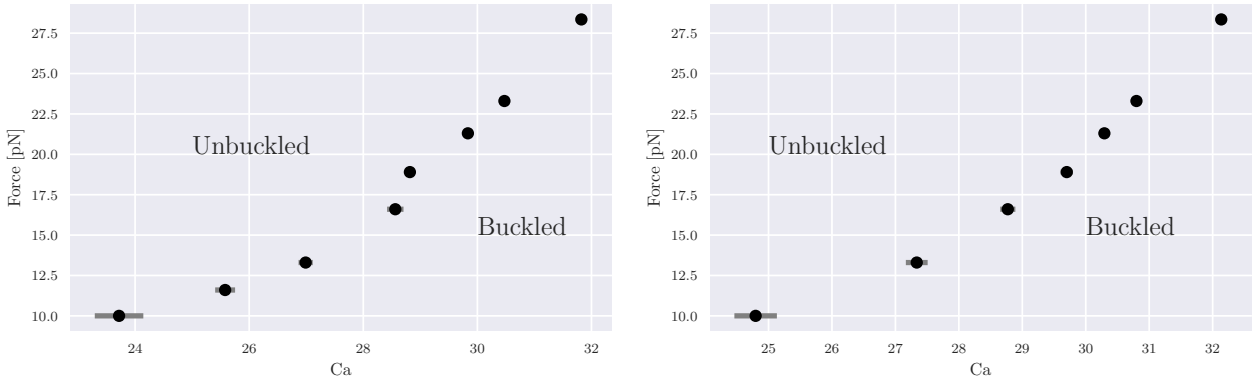

(a) (b)

Figure 5.5: Phase transition diagram for the equilater triangle configuration with base length 6σ(a), and the aligned case with base length 6σ(b).

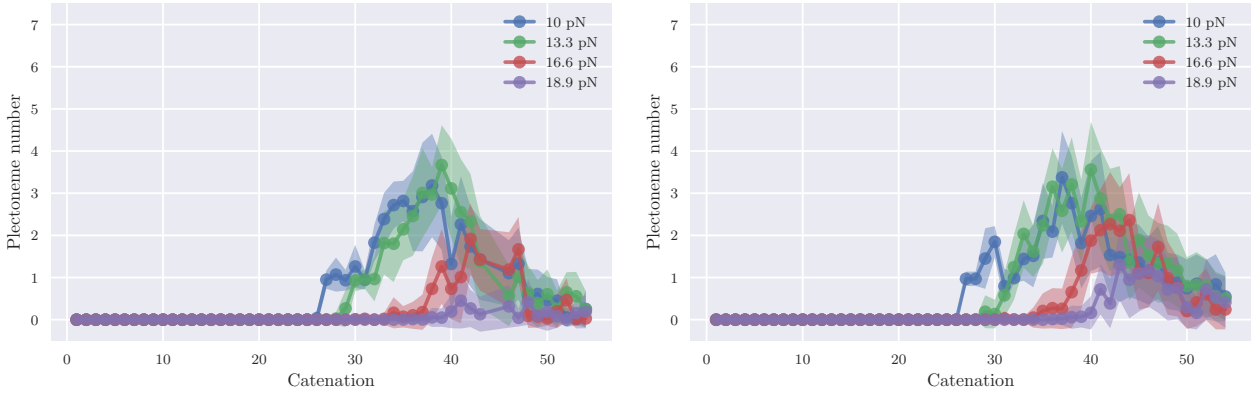

(a) (b)

Figure 5.6: Time-average detected number of plectonemes for the equilateral triangle case with base length 6σ(a), and the linearly aligned case with base distance 6σ(b).

More confirmations about these results can be obtained from the plectoneme statistics, in particular from the average number of plectonemes (figure 5.6) and the average total length (figure 5.7). Both the trends seems to be replicated between the two geometries given the statistics over which they were calculated. From these results it is possible to conclude that the change in configuration between aligned and triangular with fixed base in this case is not sufficient to induce additional effects in the statistical behavior of the system. It is possible to generalize this conclusion to triangles with different base angles, from the smaller ones between the tested cases (15°,15°) to the larger ones (70°, 80°). As it will be more clear in the following section, the change in geometry itself may not be sufficient to trigger new kind of effects. The increase in relative distance could be more effective but in this case, even for the cases with the highest base angles values (70°, 80°), it was not possible to appreciate any change.

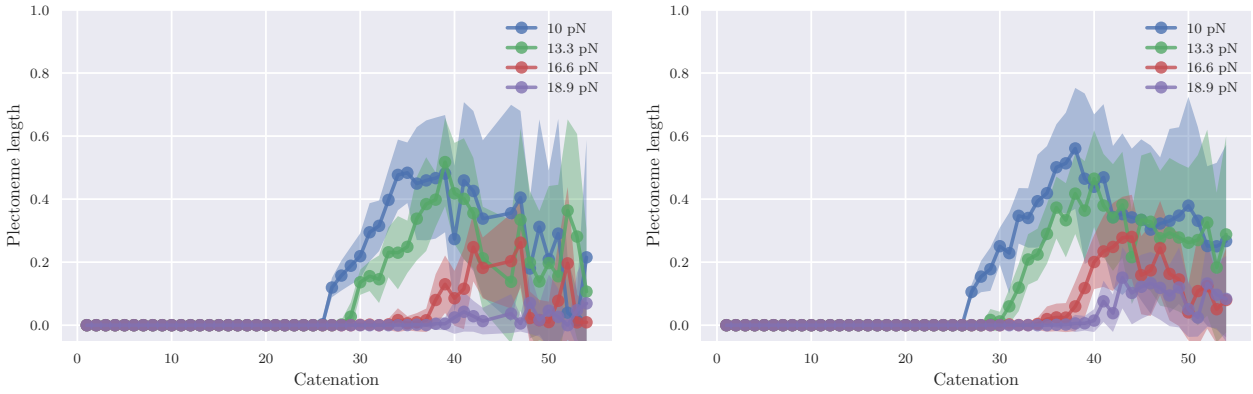

(a) (b)

Figure 5.7: Time-average cumulative plectoneme length for the equilateral triangle case with base length 6σ(a), and the linearly aligned case with base distance 6σ(b).

5.2 Comparing different configurations with base 42σ

The strong similarities between the tested triangular configurations for the 6σ case suggests us to focus on larger triangles, such as those with base length 42σ. From some early simulations done with this kind of geometry it was possible to notice at first that with small base angles the behavior was as similar to the aligned case as it was for the 6σ configurations, with almost identical results in extension, single strand writhe and plectoneme statistics.

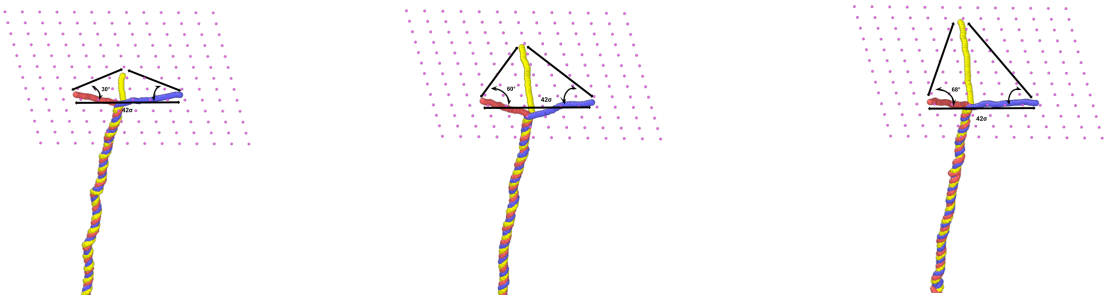

(a) (b) (c)

Figure 5.8: Braided triangular configuration (Ca=26, F=28.35 pN) with base length 42σ between red and blue strands. Base angles are 30° in (a), 60° in (b) and 68° in (c). Images tilted for visualization necessities.

Such initial confirmation of the equivalence of aligned cases to small base angle configurations brought the attention to more and more scattered triangles. The most interesting between them involved angles of 30°, 60°, 68°, depicted in figure 5.8, for which it was possible to notice the first differences. In the following sections a global comparison of these four cases will be discussed to highlight the effects of the third chain movement and possible relations between relative distance and plectoneme generation.

5.2.1 Main features

As for the already discussed cases the analysis restricted on the extension of the braid, the single strand writhe and the plectoneme statistics. By looking at the extension vs catenation graph in figure 5.9 it is possible to notice a first interesting phenomenon: as the distance between the third strand and triangle base formed by the other two strands increases the extension vs catenation plots curves move to the left. This trend finds a direct confirmation in the shifting of the catenation necessary to go through the phase transition at fixed force, that for the case with force fixed to 13.3 pN moves from 25 in the aligned case, to 20 in the case with base angles equal to 68°. Beside that the behavior is

almost equal and highlights once again the presence of a buckling transition despite the strong change in geometry.

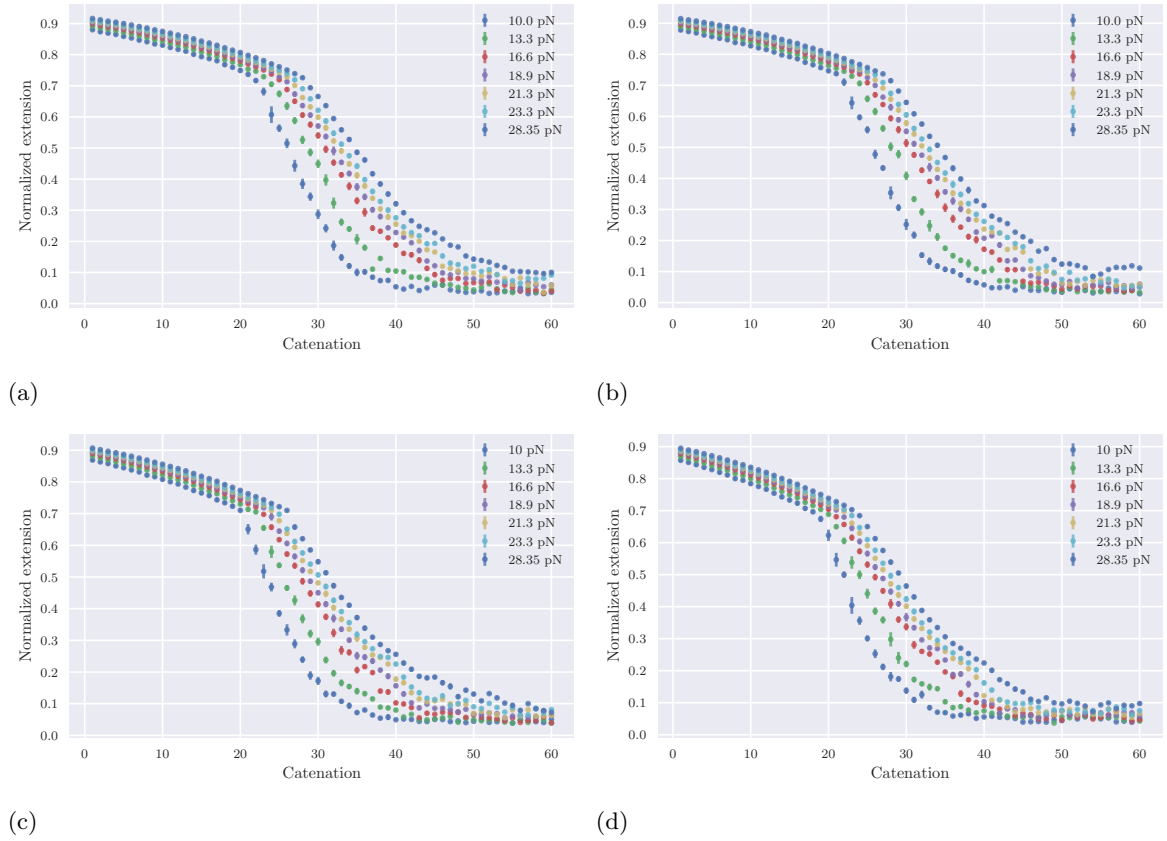

Figure 5.9: Time and strand-average end-to-end vertical distance for the triangular configurations with base length 42σ(a). Base angles are 30° in (b), 60° in (c) and 68° in (d), while (a) represents the linearly aligned configuration.

Coming to the plectoneme formation, that as discussed before has only a minor dependence on the buckling transition itself, the average number of plectonemes in figure 5.10 seems to confirm the trend. The plectoneme formation requires each time a lower catenation number, inducing a change in the critical value from a maximum of 25 to a minimum of 20 for the smallest analyzed force (10 pN). It is then possible to conclude that in the four configurations considered the change in geometry has a double effect, both on the location of the buckling transition and on the plectoneme formation.

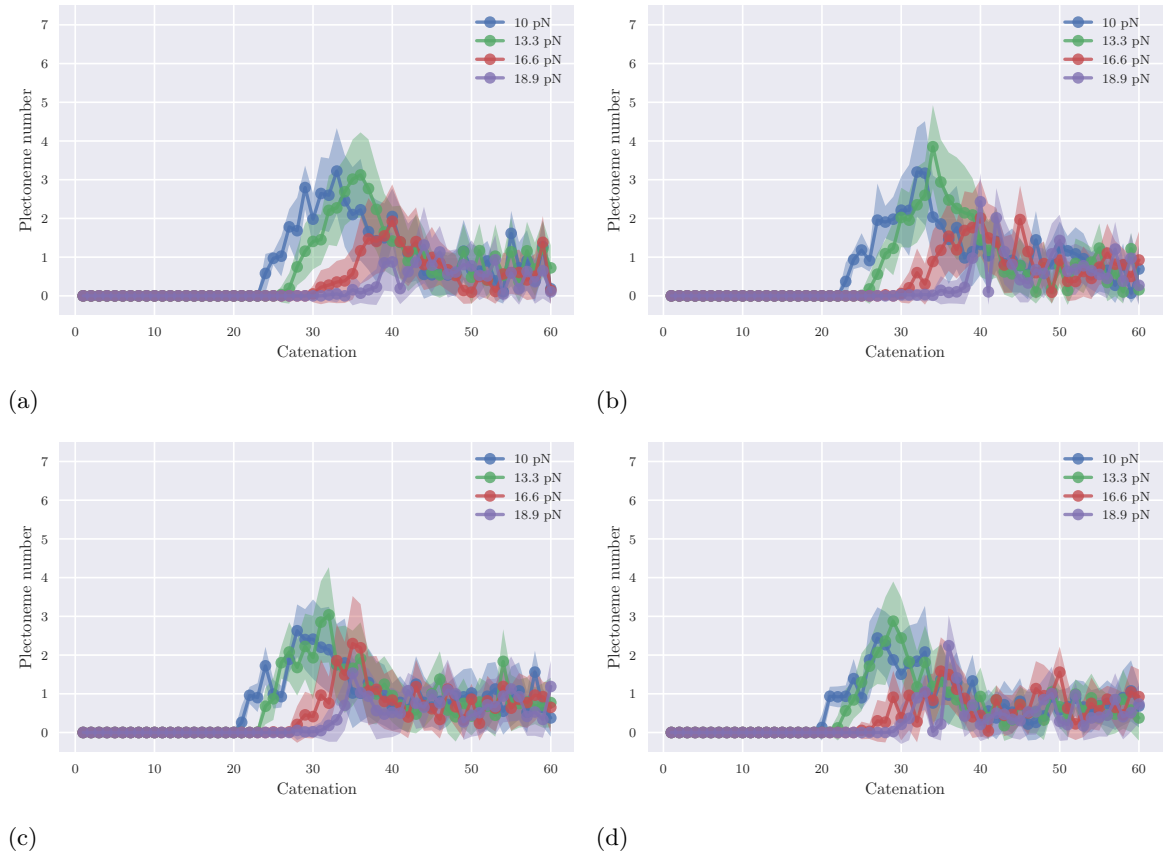

Figure 5.10: Average plectoneme number for the triangular configurations with base length 42σ(a). Base angles are 30° in (b), 60° in (c) and 68° in (d), while (a) represents the linearly aligned configuration.

5.2.2 Phase transition dependence on third chain positioning

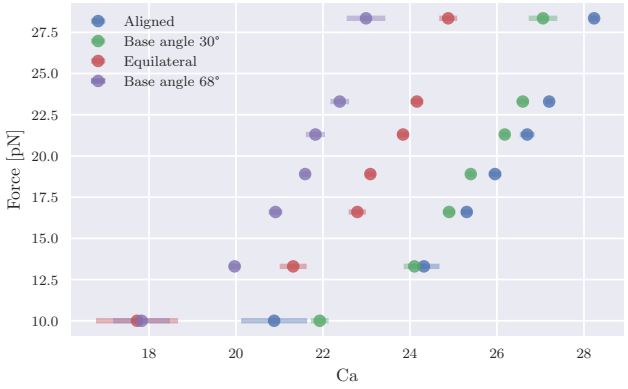

Figure 5.11: Phase transition diagram variation for triangular and aligned configurations with base length 42σ.

The phase diagrams for different cases shown in figure 5.11 highlight the already observed shift of the transition line. This kind of phenomenon seems to be directly associated to the distance of the additional chain from the triangle base, as it is present only for the configurations with the largest relative distance, while its importance increases with the base angles values.

This behavior could be directly linked to the discussed reduction of the available braiding length. As it can be seen from simulations in figure 5.8 the positioning of the third chain influences the length of the straight parts of each chain, reducing the total braid length. Such phenomenon could be critical for the buckling transition and the plectoneme formation, as the amount of stress added in such configurations, if compared to the aligned case, could ease the formation of plectonemes or solenoids by reducing the amount of catenation necessary to get non-braided conformations. To improve the knowledge of such behaviors it is necessary to investigate more deeply how plectonemes forms in such setups.

Chapter 6

Plectoneme dynamics

After having discussed in detail the average properties of the braided strands in different geometrical setups it is possible to have a general idea of how plectonemic and non-plectonemic formations are influenced by multi-stranded braid configurations. The plectoneme formation in particular has proven to be more limited if compared to the two-strands case in the same catenation settings. The reduced number and cumulative length are in fact a sign that the geometry has a large influence in these behaviors. It is possible now to focus on the structures themselves and to study both their formation and dynamics at different catenation and force settings. It will be then possible to discuss the phenomenons happening near the phase transition and deeper in the buckling phase.

The presence of a phase transition in general implies a sudden change in the presence and absence of plectonemes. Simulations instead suggested the existence of intermediate phases in which the more favorable states consists in the presence of solenoidal [11] structures instead of plectonemic ones. These two kind structures usually coexists, and sometimes alternate, with solenoids sometimes being even nucleation points of plectonemes despite the different structure and characteristics. Solenoids represent an intermediate configuration which, as it will be seen, allows to squeeze the braid's helicoidal structure. Such structures, as observed in previous chapters, are along with plectonemes responsible for the shape change in the extension vs catenation graph after the buckling transition. From such point of view these two kind of formations belongs to the same buckling phase, given that it is not possible to identify a secondary transition point in any of the studied variables.

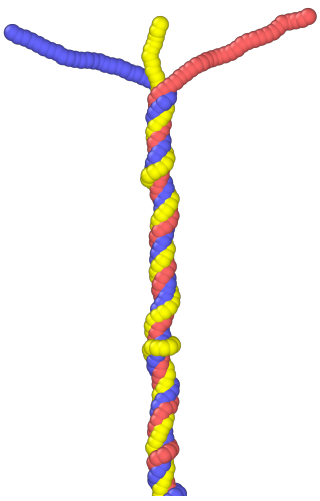

Figure 6.1: Example of non-plectonemic related coiling for an aligned configuration with base length equal to 42σ, with catenation number 26 and applied force 16.6 pN.

To improve our knowledge about these structures it is interesting to analyze the behavior near the true solenoidal-plectonemical transition, instead of the old buckling transition, in order to understand

how continuous the passage is. While exploring the middle phase it is possible instead to observe the old plectonemic structure in a new fashion, and finally, for larger catenation numbers, observe strange globular complexes obtained as a result of the stressed braid. Kymographs present in this chapter are showing the plectoneme positioning and displacement and are obtained using the detection method discussed in chapter 4. Their accuracy varies a lot depending on the studied configuration, showing that more efforts should be done to improve the detection method, in particular to avoid losing track of plectonemes in highly packed braids.

6.1 Dynamics close to the buckling phase transition

6.1.1 Base size 6σ

Given the substantial equivalence between all the discussed cases with base length 6σ it is possible to discuss a single case (the linear aligned one) and share the conclusion with all the others. From now on all the presented results will use then as a reference the aligned case that, as discussed in chapter 4, has the most general behavior.

The first expected results, present both in simulation visualization and plectoneme detection, is that the plectonemes manifest themselves only with catenations larger than the ones calculated theoretically for the buckling transition. For example in the case with forces equal to 16.6 pN the lower theoretical bound for the buckling transition is estimated to be ≈ 29 while the first plectoneme is detected instead at $Ca = 35$. This effect becomes interesting when a group of plectonemes is required to be stable in time, and this happens approximately around the catenation number of 40 and slightly higher values. Near the theoretical phase transition instead plectonemes are very uncommon, with the braid slowly transitioning into a completely solenoidal configuration. The buckling transition studied in the previous sections seems more to represents a theoretical bound beyond which the plectonemic structures can appear (and do with very small statistics) than a true bound to overcome in order to have the plectoneme appearance certainty.

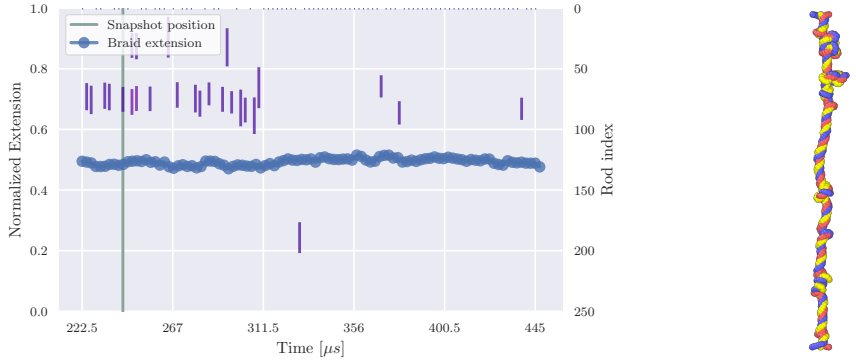

(a) (b)

Figure 6.2: (a) Plectoneme kymograph at force 16.6 pN and catenation 36, in blue the average braid extension, in purple plectoneme positioning and length. (b) Plectoneme structure at time $\approx 242\mu s$.

The phenomenon intensity becomes very interesting with larger forces, such as 31.95 pN. By increasing the catenation number to get through the transition line and deeper inside the buckling phase it is possible to notice that the plectoneme appearance is more and more uncommon, leaving a zone in which the main events are associated to the solenoidal formations. In general as observed in figure 4.10 it is possible to conclude that by increasing the force the catenation number required to find plectonemes gets higher and higher, while for large forces (> 23.3 pN) plectonemes can hardly be found.

6.1.2 Base size 42σ

As discussed in previous chapters the dynamics in the four discussed cases with base length fixed to 42σ are very similar in behavior, but not in phase transition displacement. For each discussed case in fact, the only phenomenon that happens when crossing the theoretical phase transition line is the creation of already noticed solenoidal structures. To see real plectoneme formation it is necessary to further increase the catenation number, as already discussed in chapter 4 with reference to 5.8.

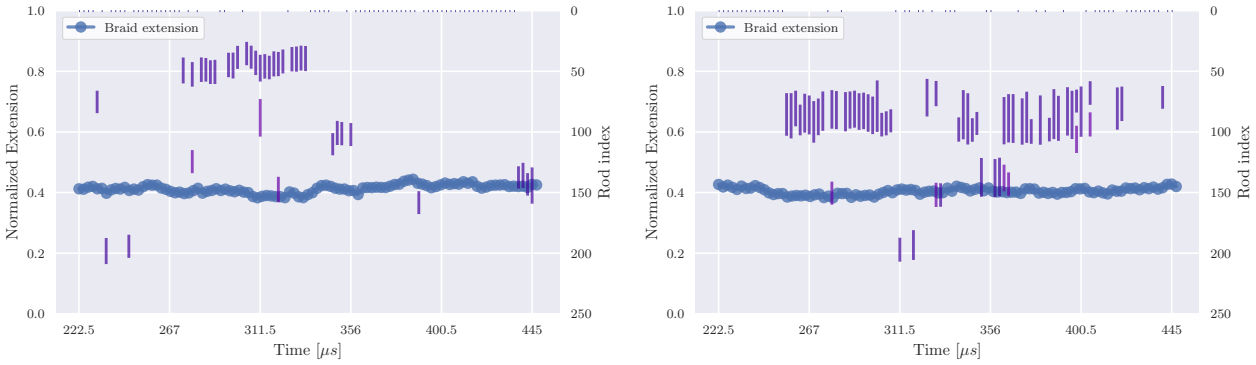

(a) (b)

Figure 6.3: Plectoneme kymograph, in blue the average braid extension, in purple plectoneme positioning and length. In (a) the base length is fixed at 42σ, the force is 16.6 pN, the catenation is 33, and the arrangement of the 3 anchored ends is linear, while in (b) the configuration is equilateral, the force is 16.6 pN and the catenation is 30.

The plectoneme dynamics in figure 6.3 shows that between the different setups, the effect of the structure change has a large influence in the plectoneme appearance (see figure 5.10), but also on the dynamics. It is possible in fact to get the same dynamics by slightly decreasing the catenation number if we take into account the linear and equilateral configurations as done in figure 6.3. The configuration change has made possible to get a similar behavior (with even larger plectonemes) for the price of moving the third chain away from the other two. For what concerns the appearance of plectonemes the behavior near the real plectonemic transition seems to be truly random with continuos jump between positions on the braid and disappearances to the braided/solenoidal state. This kind of instability may be associated to the continuity between the solenoidal and plectonemic phases, and the fact that such structure may interchange each other without any real jump between the first and second form.

6.2 Dynamics in the middle of the plectonemic phase

In chapter 4 and 5 the number of plectonemes has been proven to increase up to a certain catenation number and then decreasing again, leaving room to a completely different set of behaviors. The maximum number of plectonemes is obtained at intermediate catenation numbers, and may be studied to compare the new plectonemic dynamics to the old one and see if it presents the same set of characteristics.

6.2.1 Base size 6σ

A first example of the dynamics in a 6σ setting can be observed in figure 6.4 where the number of plectonemes has clearly increased if compared to the same analysis performed in proximity of the transition. The size of plectonemes increased too from previous cases, while it possible to observe examples of liquid-gas phenomenons [30] such as merging, fusion, fission or Ostwald ripening. It is possible in fact to notice fusion processes, especially for the first two detected plectonemes it is possible to see a merging phenomenon in which two plectonemes becomes more and more close to each other to form a single one.

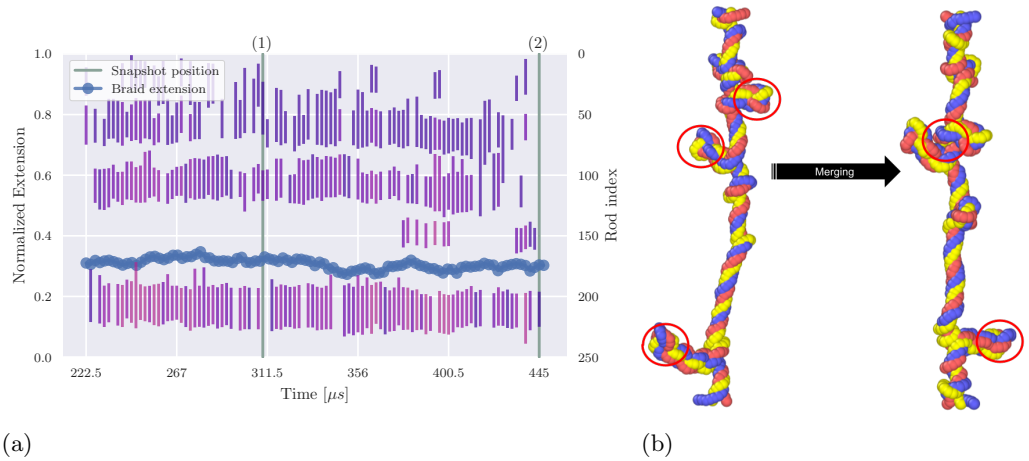

Figure 6.4: (a) Plectoneme kymograph at force 13.3 pN and catenation 37, in blue the average braid extension, in purple plectoneme positioning and length. (b) Plectoneme structure at time $\approx 309\mu s$ and time $\approx 445\mu s$.

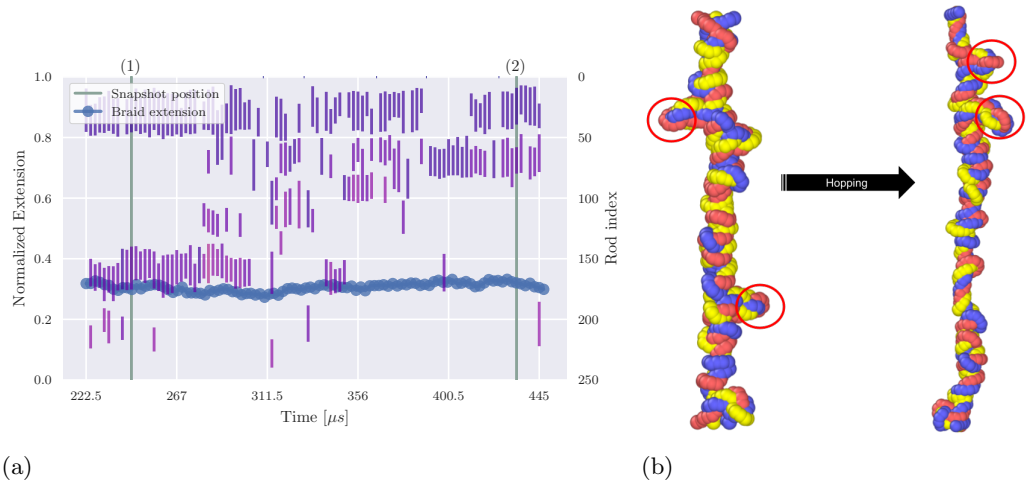

Figure 6.5: (a) Plectoneme kymograph at force 16.6 pN and catenation 40, in blue the average braid extension, in purple plectoneme positioning and length. (b) Plectoneme structure at time $\approx 245\mu s$ and time $\approx 434\mu s$.

In a second discussed case (figure 6.5) it is possible to notice instead the hopping of a plectoneme as a jump in position of one of the two plectonemes appearing in the configuration. This phenomenon has some experimental evidences [8], and consists in the disappearance from the original position and the formation in another site and can be correlated with the energy necessary for the nucleation of a new plectoneme and the rotation of intermediate DNA. For higher forces, as underlined in the discussion of the previous chapters, the number of plectonemes decreases while the instability arises. The amount of solenoidal components of the braids in fact increases with the force, reducing to a minimum the plectonemic activity.

6.2.2 Base size 42σ

Configurations with larger base sizes are expected to undergo the same kind of behavior at intermediate catenation numbers. The increase in distance of the third strand attachment point is expected to influence the dynamics by reducing in particular the total amount of plectonemes present during the simulation, as already observed in previous chapters.

The first test discussed in the section (figure 6.6) concerns an "aligned" configuration with low force. The resulting dynamics is very similar to what was found in the previous section, with a fission process for a plectoneme in the first stages of the simulation and then a fusion at the end. The render in figure 6.6(b) allows understanding better the state of the braided configuration and highlights the amount

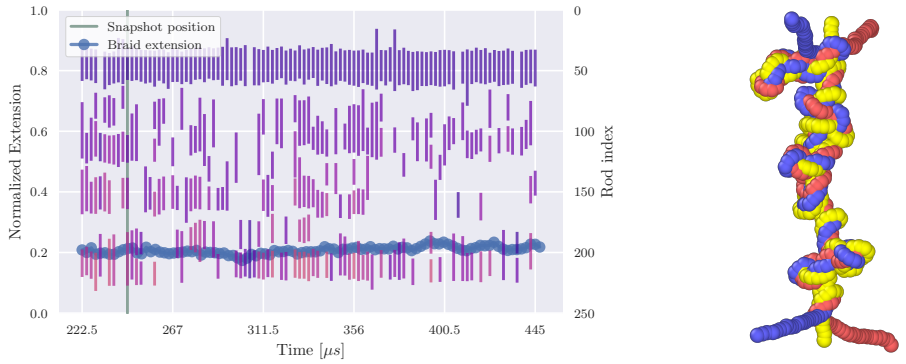

(a) (b)

Figure 6.6: (a) Plectoneme kymograph at force 13.3 pN and catenation 35, in blue the average braid extension, in purple plectoneme positioning and length. (b) Plectoneme structure at time $\approx 245\mu s$.

of solenoidal structures presents in the system, with the plectonemic structures barely distinguishable from the rest of the braid.

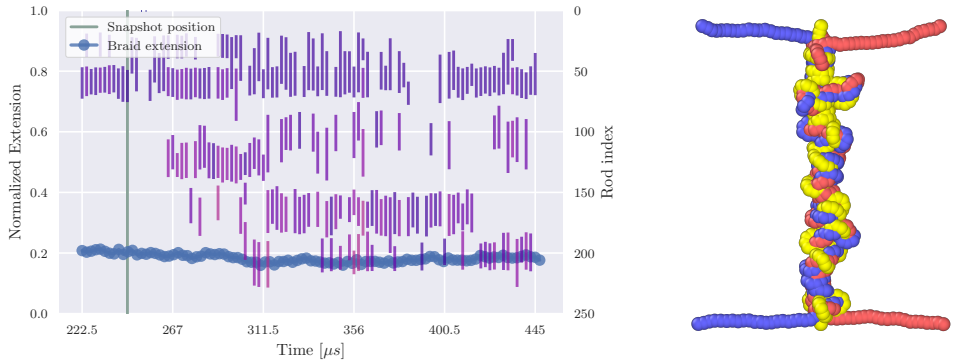

(a) (b)

Figure 6.7: (a) Plectoneme kymograph at force 16.6 pN and catenation 40, in blue the average braid extension, in purple plectoneme positioning and length. (b) Plectoneme structure at time$\approx 245\mu s$.

With higher forces, as in figure 6.7 the situation is more critical with a reduction in the total number of plectonemes and an increase in hopping phenomenons, probably eased by the amount of solenoidal structures. Globally the plectonemes seems to be more disordered and barely distinguishable from the central braided/solenoidal structure, with the dynamics being directly influenced by this configuration, in which transitions between nucleation points and plectonemes are eased and really frequent.

Setups with larger base angles such as the one in figure 6.8 seems to be associated instead to a more chaotic behavior. The number of plectonemes is in fact reduced, and the braid becomes very short if compared to previous configurations. However, it is possible to detect the plectonemes and even see them directly by visualizing the simulation, but it can be noticed how the braided phase is slightly leaving room to a more packed displacement of the strands.

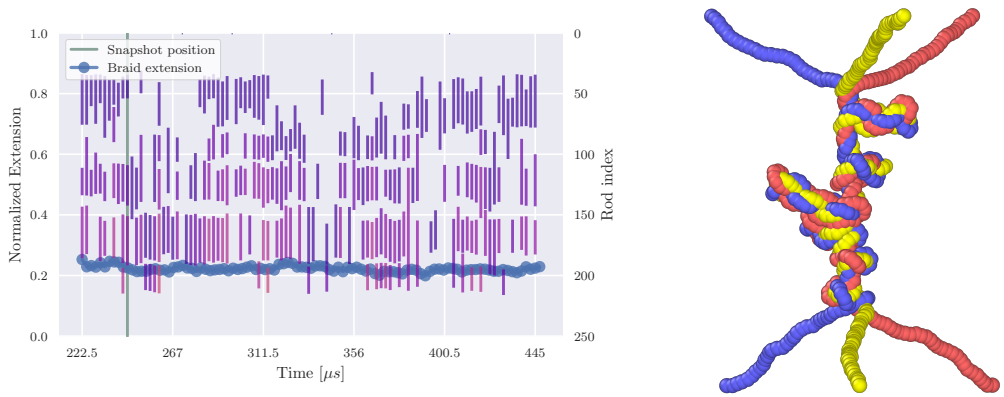

(a) (b)

Figure 6.8: (a) Plectoneme kymograph at force 13.3 pN and catenation 30, in blue the average braid extension, in purple plectoneme positioning and length. (b) Plectoneme structure at time$\approx 245\mu s$.

6.3 Dynamics deep in the plectonemic phase

The progressive increase in the catenation number has a direct effect on the way the braid is coiled. The stress added by the rotations constrains the braid to reduce its extension and buckle in a globular conformation in which plectonemes (but also solenoids) are very difficult to be detected. This kind of globular configuration represents an extreme case of supercoiling that characterizes each tested configuration if the catenation number is large enough. The study of dynamics is really limited, and sometimes it is only possible to observe this highly packed configuration without any further analysis.

6.3.1 Base size 6σ

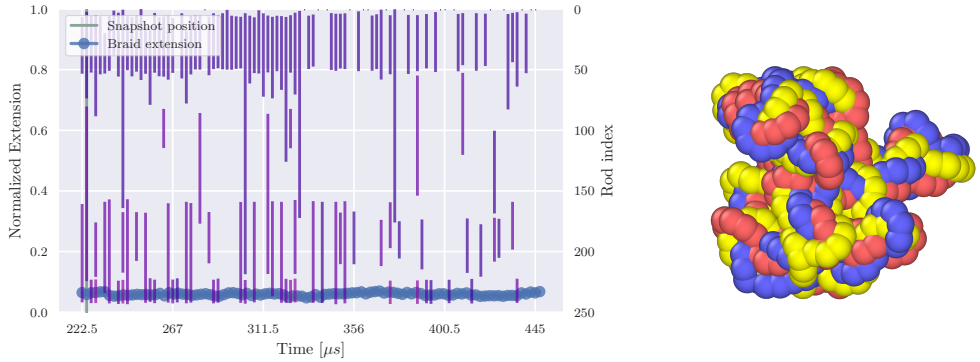

(a) (b)

Figure 6.9: (a) Plectoneme kymograph at force 13.3 pN and catenation 48, in blue the average braid extension, in purple plectoneme positioning and length. (b) Plectoneme structure at time $\approx 225\mu s$.

In cases such as the one presented in figure 6.9 the braid compression makes it very difficult to correctly detect the plectonemes. These are in fact hardly located even by eye, since they can be easily confused with the rest of the globular structure. The automatic detection in this case may or may not be reliable or even not classify correctly the plectonemes, being them impossible to define in such configurations.

With higher forces, as in figure 6.10 the situation seems to improve slightly, with a less compressed braid, but with the same recognition problems. The tested algorithm seems so to detect a very large range of plectonemes, while the instability is pretty clear, with their sudden creation and disappearance. Again, due to the globular and chaotic structure it is very difficult to confirm such analysis, even through renders, or even affirm that plectonemes are currently present in such configurations, so results may be considered with caution.

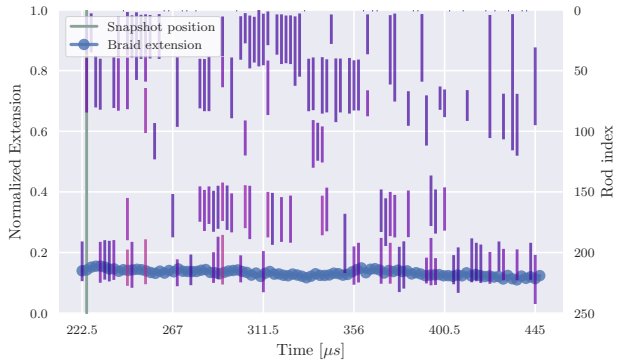

(a) (b)

Figure 6.10: (a) Plectoneme kymograph at force 16.6 pN and catenation 48, in blue the average braid extension, in purple plectoneme positioning and length. (b) Plectoneme structure at time $\approx 225\mu s$.

6.3.2 Base size 42σ

The configuration status with base sizes of 42σ is very similar to what was seen in previous examples. In figure 6.11 the structure is again really compressed, with a very small braid size and some difficulties in locating plectonemes both by eye and through the developed algorithm.

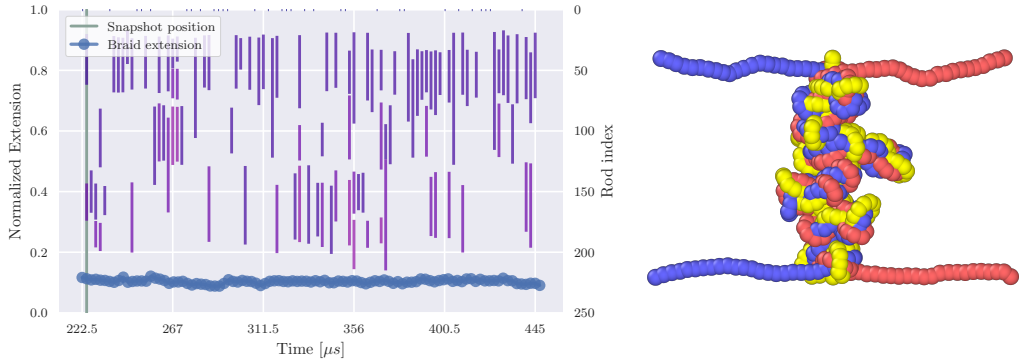

(a) (b)

Figure 6.11: (a) Plectoneme kymograph at force 13.3 pN and catenation 41, in blue the average braid extension, in purple plectoneme positioning and length. (b) Plectoneme structure at time $\approx 225\mu s$.

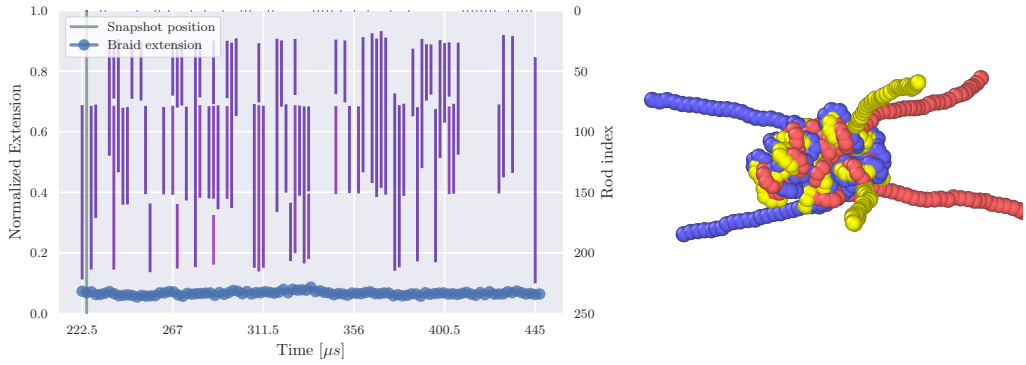

(a) (b)

Figure 6.12: (a) Plectoneme kymograph at force 13.3 pN and catenation 39, in blue the average braid extension, in purple plectoneme positioning and length. (b) Plectoneme structure at time $\approx 225\mu s$.

For configurations with larger base angles, the concept of plectoneme loses meaning, and what we can see is a single conglomerate of strings completely coiled around themselves. In figure 6.12 the braid has become a single globular complex without any meaningful states, both braided or plectonemic. In conclusion it is safe to assume so that such states are impossible to study and probably irrelevant for any analysis aimed at the plectonemic characterization.

Chapter 7

Relaxing from three to two chains

After having discussed the characteristics of the three braids systems at equilibrium it is now possible to make an attempt at analyzing braided strands moving from 3-chains configurations to the 2-chains ones. The focus will be on situations in which a bond inside the third strand (the newly added one) eventually breaks, and the resulting sub-chains are free to move in the space independently. A fraction of the stress is released, allowing the configuration to relax to the 2-chain state expected for that Ca and F.

In practice the introduction of the bond breaking was done through LAMMPS by removing completely the bond and the angle interactions around the breaking point, that for all the discussed cases is localized in the middle of the interested chain (see appendix A). For what concerns instead the simulated cases, only the configurations with distance between anchoring points equal to 42σ were considered, in particular the linearly aligned one and the case with base angles fixed at 68°. The force was fixed to 13.3 pN, a value that allows to get the largest population of plectonemes (see figure 5.10).

7.1 Unbuckled to unbuckled relaxation

The first relaxation dynamics considered is due to a quench from the unbuckled phase of the 3-chains system to the unbuckled phase of the 2-chains case (see inset of figure 7.1(a)). Given that the catenation number to reach the transition for the three chain configuration is required to be much smaller for braids than for the 2-strands configuration, it is always possible to reach a 2-chains unbuckled state from a 3-chains unbuckled state since it is sufficient to pick a small enough catenation number given the pulling force.

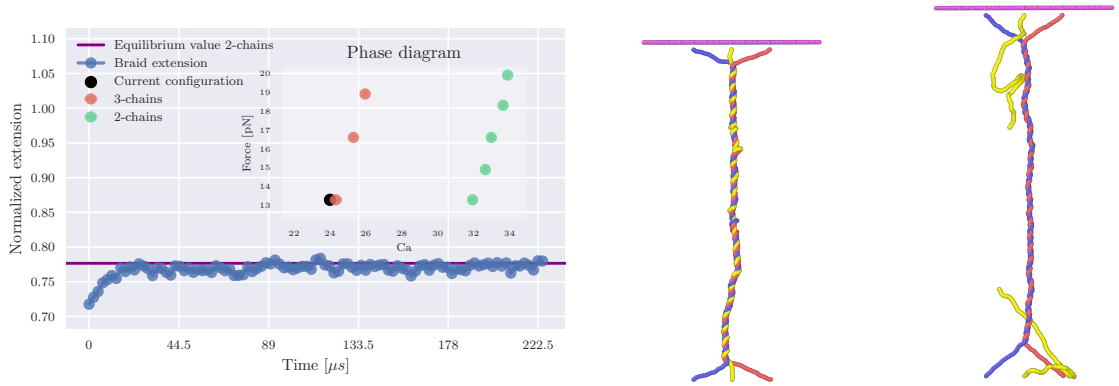

(a) (b)

Figure 7.1: (a) Extension variation of the configuration after the bond breaking for the linear case. (b) Braid configuration change from the beginning of the simulation to the equilibrium state. Catenation number fixed at 24, pulling force 13.3 pN.

As it is possible to notice from figure 7.1, the bond breaking allows the system to relax in a relatively small time (less than 255 μs), to the 2-strands configuration even in presence of the two subchains originated by the cut chain. The disturbance on the remaining braided strands seems to be irrelevant to the relaxation process.

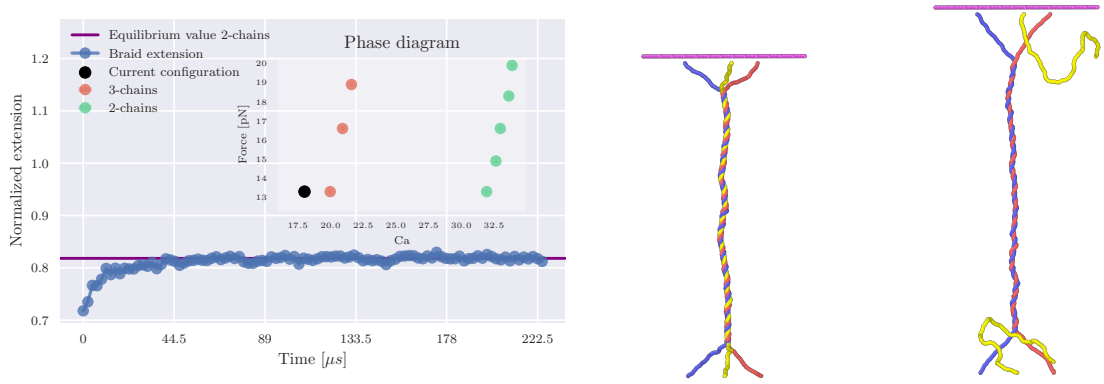

(a) (b)

Figure 7.2: (a) Extension variation of the configuration after the bond breaking for the triangular case. (b) Braid configuration change from the beginning of the simulation to the equilibrium state. Catenation number fixed at 18, pulling force 13.3 pN.

Similar results can be obtained with a triangular geometry, as the one discussed in figure 7.2, with an even faster relaxation to the equilibrium from a shorter extension. This result may be a consequence of the third strand positioning, that could ease the movement freedom and ability to untangle the braid.

7.2 Buckled to unbuckled relaxation

More interesting results are observed when the cut occurs inside the plectonemic phase. The sudden breaking of the third chain influences the structure stability and rapidly disentangles the already formed plectonemic structures. During the relaxation the third chain sweeps away from the plectonemes and begins to fluctuate around the newly formed braid. Sometimes it remains stuck in between the other two strands and forces the formation of plectonemes (formed alternatively by two or three strands), but this transient state seems to last only a fraction of the total time.

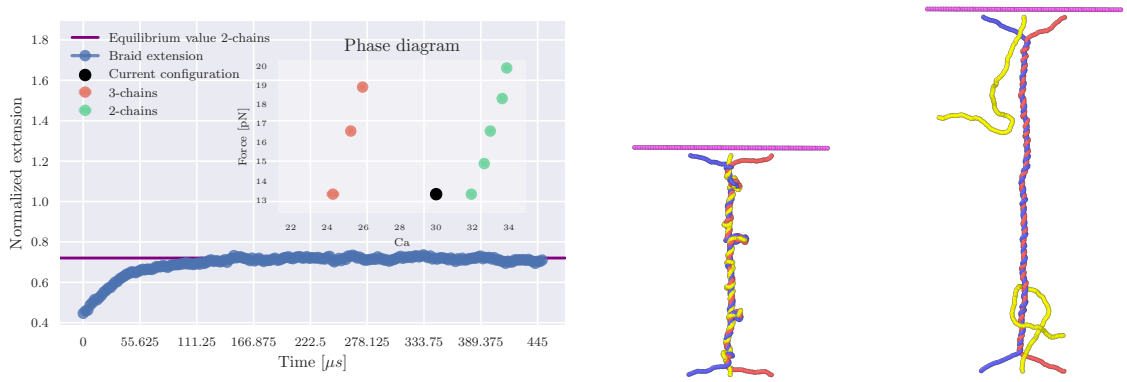

(a) (b)

Figure 7.3: (a) Extension variation of the configuration after the bond breaking for the linear case. (b) Braid configuration change from the beginning of the simulation to the equilibrium state. Catenation number fixed at 30, pulling force 13.3 pN.

In the first analyzed case in figure 7.3, with catenation number 30 and aligned configuration, the

relaxation to the stable 2-strands state requires more time than what was observed in previous cases, probably because the third strand remain tangled with the other two for a larger amount of time. The final state instead doesn't present any of these criticalities since it is energetically equivalent to a simple two strands unbuckled state.

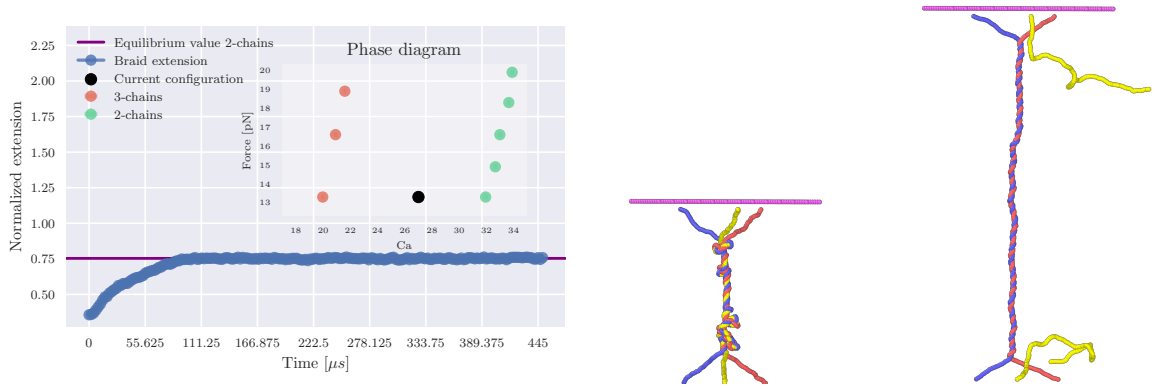

(a) (b)

Figure 7.4: (a) Extension variation of the configuration after the bond breaking for the triangular case. (b) Braid configuration change from the beginning of the simulation to the equilibrium state. Catenation number fixed at 27, pulling force 13.3 pN.

The triangular configuration in figure 7.4 has instead a smaller catenation number and in fact needs a smaller time to equilibrate. The disentangling is eased in this case by the lower coiling of the strands, with the third chain able to sweep and reach a movement freedom faster. Moreover, while the initial configuration presents a great amount of both solenoidal and plectonemic conformations the final structure does not show anything similar when returning to the unbuckled original 2-strands configuration.

7.3 Buckled to buckled relaxation

Finally, the relaxation from the 3-chains buckled to the 2-chains buckled phase can be considered. In this case the catenation is sufficient to generate plectonemic or solenoidal structures in both the 3-strands and 2-strands configurations. The dynamics allows to see these conformations rapidly evolving and turning the packed structure into a longer one, with the generation of plectonemic structures during all the relaxation time.

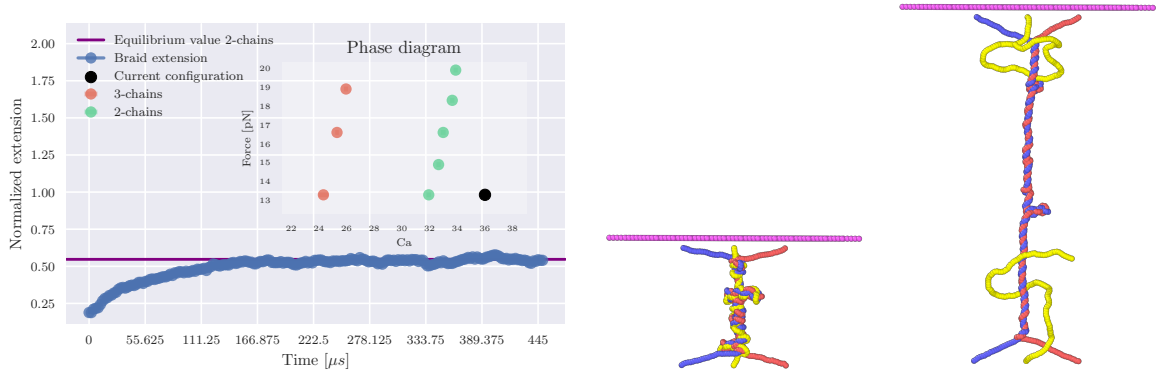

(a) (b)

Figure 7.5: (a) Extension variation of the configuration after the bond breaking for the linear case. (b) Braid configuration change from the beginning of the simulation to the equilibrium state. Catenation number fixed at 36, pulling force 13.3 pN.

In the aligned case in figure 7.5 the relaxation time becomes very long. It requires more than 200 μs to get an equilibrium configuration, and this may be associated again to the high coiling of the system. When relaxed and during the process the braid made up by the remaining two strands forms as expected lot of plectonemes that are usually observed when dealing with simple 2-chains configurations. In this case more than others it was possible to observe the mixed plectonemes that were already appreciated during previous simulations.

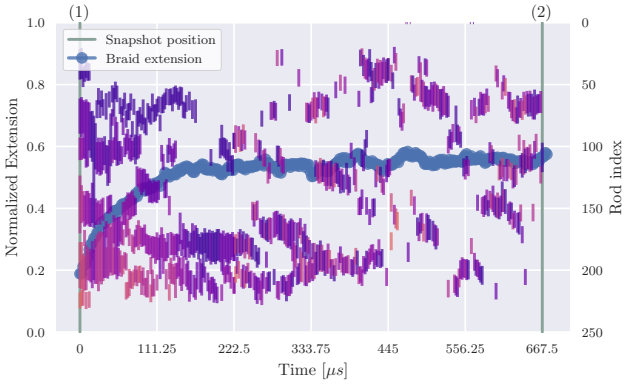

Figure 7.6: Plectoneme kymograph for the linear case at force 13.3 pN and catenation 36, in blue the average braid extension, in purple plectoneme positioning and length. Snapshot positions refers to figure 7.5.

For what concerns the plectoneme dynamics, it is possible to analyze its behavior using the already discussed methods. In particular, being a 2-chains configuration for most of the simulation, the original method exploiting the contact maps can be considered sufficient to get a good detection of the plectoneme formations, even if the presence of the third chain can contribute with a significative disturbance. The dynamics in figure 7.6 shows a brief persistence of original plectonemic structures in the transient phase, which, once reached the equilibrium, participate in the usual 2-strands dynamics with hopping and merging phenomenons. The original plectonemes seems so to be caught in this dynamics by being conserved even after the equilibration or by being dismantled and absorbed in the braided part of the 2-strands configuration.

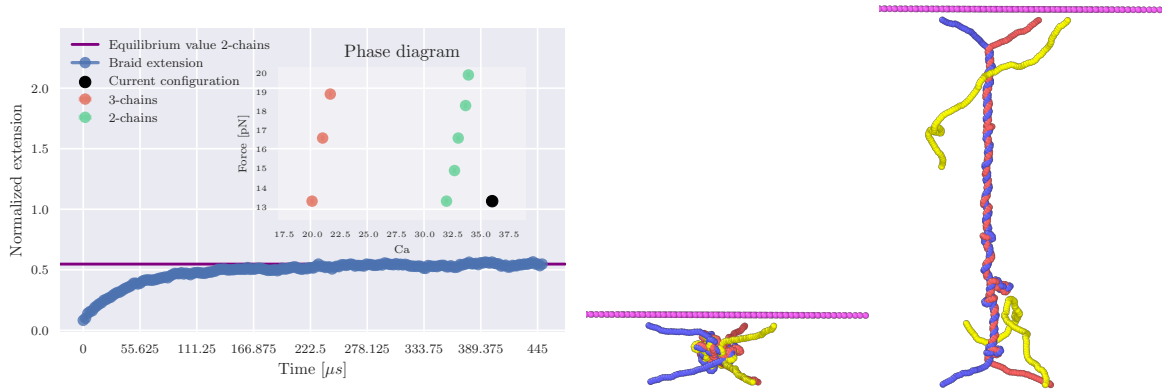

(a) (b)

Figure 7.7: (a) Extension variation of the configuration after the bond breaking for the triangular case. (b) Braid configuration change from the beginning of the simulation to the equilibrium state. Catenation number fixed at 36, pulling force 13.3 pN.

In the triangular configuration (figure 7.7) the structure has already become globular and very small. Despite this, both the extension profile and the two renders shows how the system is free to get rid of such limits and return to the original state, as was already discussed for the case in figure 7.5. It is also noticeable that the two processes require a similar time, even if the starting configurations are really different.

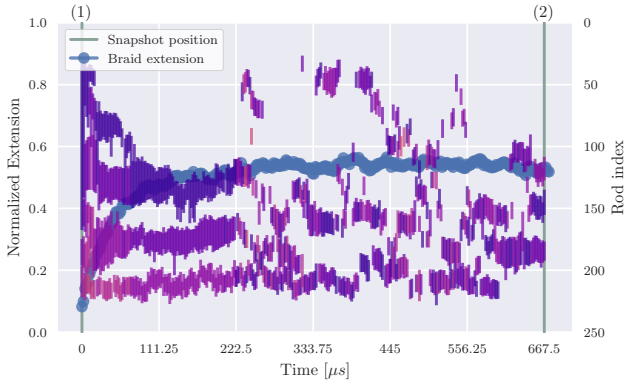

Figure 7.8: Plectoneme kymograph for the triangular case at force 13.3 pN and catenation 36, in blue the average braid extension, in purple plectoneme positioning and length. Snapshot positions refers to figure 7.7.

As for the linear configuration, similar plectoneme dynamics can be observed for the triangular configuration in figure 7.8. Despite starting from a globular configuration, the contact map method seems to detect some plectonemes in the initial structure and in the first simulation steps, when the braid starts to expand and relax. These plectonemes resist during the transient phase, with a single episode of merging reducing their total number, while leaving room once again to the usual plectonememe dynamics for 2-chains cases when the system is finally relaxed.

Chapter 8

Conclusions

The aim of this work was to expand the knowledge on braided systems subject to torsional and elongational forces, by including configurations with multiple strands, inspired by their possible outcomes [20]. The focus in particular was centered on discussing quantitatively and qualitatively the presence of buckled structures along the braid formed by three strands. Previous works [17] evidenced that by applying small pulling forces and high catenation numbers on two strands braids it is possible to observe the formation of plectonemes with different statistics and behavior. In this thesis, by adding a third strand to the system and testing different anchoring geometries it was possible to observe new and interesting behaviors, involving both the plectoneme dynamics and statistics.

At first, with the third chain inserted in between the original two, it was possible to notice that the buckling transition was present as in the 2-strands case, but with a shifted transition curve. In fact the shape change of the extension vs catenation plot appears for catenation numbers smaller than the one observed in the 2-strands cases. This result is also true when one looks at the writhe vs catenation curve, while the plectoneme statistics is subject to a really important change. Plectoneme formation seems in fact to be restricted to a small set of catenation numbers and forces, while the number of plectonemes is on average smaller than the one obtained in the 2-strands cases. Finally, these behaviors do not depend on the anchoring, having different distance geometries.

To expand this analysis the displacements of the strands were changed. From aligned cases the analysis moved on configurations with a triangular displacement of the docking points, getting for the smallest distances the usual behavior, while largest distances triggered new and interesting results. It was in fact possible to observe very similar dynamics by changing the docking point of the newly added chain, but each time the critical catenation decreased as the distance of the anchoring point moved further from the base of the triangle made by the extremities of the two original strands. This result is possibly due to the reduced braid length, influenced by the non-braided part of the newly added chain, becoming longer and longer.

After having discussed the main statistical properties of the system of interest, we focused on the dynamics of the buckled structures along the braid. The presence of non-plectonemic structures such as solenoidal-like ones hampered the detection of plectoneme using the contact map method, which were integrated with the local computation of the single-strand writhe. This allowed computing precisely the behavior of plectonemes in many configurations, and rediscover phenomenons such as merging and hopping of plectonemes that were previously found in other works. Finally, for sufficiently high catenation numbers it has also been possible to observe a "globular" phase, with the braid being squeezed in a very small space.

As a last test it was possible to observe the relaxation of the system from 3-strands cases to 2-strands ones. This was done by breaking the bond between two beads for the third chain and letting the system relax back to the 2-strands case. Results obtained from such tests showed the substantial equivalence of the resulting configurations with the already tested two chain cases, as expected since the newly added strand should not influence the braid dynamics once broken.

The characterization of the cases in which three strands braids allowed to enlarge our knowledge of how braiding could work on systems more complex than the ones already tested, but many details were still not precisely defined. The crossover between solenoids, plectoneme and globular states is very difficult to characterize as a phase transition, since they seem to belong to a unique buckled state in the force/catenation plane. The transition in fact takes place in the extension vs catenation plot for a single point at fixed force, where the shape of the diagram suddenly changes. It has not been possible to observe such clear evidences for the other discussed cases, for which it is also possible to observe coexistence between the different possible structures. Moreover, this simultaneous presence of plectonemes and solenoids makes it very difficult to detect plectonemes, and more precise methods should be developed to get the best possible correspondence between the structures present and detected. This could be done for example, by studying the braid centerline and its properties. Such techniques may be associated to a more accurate analytical model, able to discriminate successfully the different structures that could be created in the buckled state. The study of braid pitch and radius can be, as in previous models [13] the key to express such kind of behavior in an energetic fashion and explain the observed phenomenons. Finally, a focus on the phase diagram variation associated to the displacements of the third chain in some cases (see chapter 5), could also be integrated in such models, explaining how the free energy of the system is influenced by geometrical changes.

Appendices

Appendix A

LAMMPS Code

LAMMPS (*24Mar22*) [19] was the main applicative used during the work, through which it was possible to accurately simulate the required systems. After having generated the three strands and the wall with *python* [31] as a set of beads positions, they were loaded and then simulated in order to study the braid behavior.

After having the initial structure was available, the potentials were directly implemented by dividing the system in 4 kinds of atoms, a type for each chain and a last one for the wall with the already discussed characteristics, including a lower mass (0.001).

```
# Initialization
units       lj
boundary    p p p
atom_style    angle
read_data    ../../3chains/inputs/${kindofbase}-${d}d/${d}d.lk${templk}.lmp
neighbor 10.3 bin
neigh_modify every 1 delay 1 check yes

# Define groups
group       chain1  type 1
group       chain2  type 2
group           chain3  type 3
group           all     union chain1 chain2 chain3
group     upperwall type 4
group     upperatoms id 1 251 501
group     downatoms id 250 500 750
group     rotatingbeads union upperwall upperatoms
group     pulledbead id 751
group     others subtract all upperatoms

# Potential information

pair_style      lj/expand 1.1224615296218
pair_modify     shift yes
pair_coeff  1 1 1.0 1.0 0.0
pair_coeff  1 2 1.0 1.0 0.0
pair_coeff  1 3 1.0 1.0 0.0
pair_coeff  1 4 1.0 1.0 3.3673845888654
pair_coeff  2 2 1.0 1.0 0.0
pair_coeff  2 3 1.0 1.0 0.0
pair_coeff  2 4 1.0 1.0 3.3673845888654
pair_coeff  3 3 1.0 1.0 0.0
pair_coeff  3 4 1.0 1.0 3.3673845888654
pair_coeff  4 4 1.0 1.0 6.7347691777308


bond_style    fene/expand
bond_coeff    1   30.0   1.5   1.0   1.0   0.0
```

```
special_bonds fene

angle_style    cosine
angle_coeff      1 20.6
```

Listing A.1: Potential implementation

The first step to prepare the system consisted into the rotation of the initial configuration in order to generate the different catenation initial states.

```
fix        2 others     langevin 1. 1. 2. 212112
fix      3 downatoms setforce 0.0 0.0 0.0
fix      4 others     wall/region wall     harmonic 200.0 1.0 1.0
fix        5 pulledbead  smd cfor ${force} tether NULL 258.0 NULL 0.0
fix      6 rotatingbeads rigid group 1 rotatingbeads force 1 off on off torque 1 off off
     off  # rigid fix on the upper beads and wall

variable tname loop 0 1000

    label rot_loop

    fix          7   rotatingbeads   move  rotate 0.0 0.0 0.0 0.0 10 0.0 ${period} #
    rotating the upper part as a rigid body
    run  20
    unfix        7
    run  1

    next tname
    jump SELF rot_loop

# settings for a working output file
velocity all set 0 0 0
```

Listing A.2: Rotation code for three chains case

The rotation process is performed through the use of "rotate" command of LAMMPS by considering the upper beads of the different strands and the wall. The rotation process involves a rigid rotation along with some time instants in which the system is equilibrated. This allows to avoid getting too large bonds or geometrically wrong configurations.

After having generated such braided configurations it was possible then to proceed with the equilibrium simulation at fixed temperature.

```
  label mainloop
  # Generating file for trajectory
  dump         1    all    atom    ${times_dump}   ../../3chains/dumps/${kindofbase}-${d}d/
    dump.N250.Lk${lk}.f${pnForce}.${tname}.lammpstrj


  # Dynamics
  fix        1 others     nve
  fix        2 others     langevin 1. 1. 2. ${tseed}
  fix      3 downatoms setforce 0.0 0.0 0.0
  fix      4 others     wall/region wall   harmonic 200.0 1.0 1.0
  fix        5 pulledbead  smd cfor ${force} tether NULL 258.0 NULL 0.0
  fix      6 rotatingbeads rigid group 1 rotatingbeads force 1 off on off torque 1 off
    off off
  run        ${times_force}

  next tseed
  next tname
  undump 1
  jump SELF mainloop

clear
```

Listing A.3: Simulation at fixed temperature

The force was imposed through the "smd" command, while the wall was rigidly fixed and only able to move upwards and downwards. The lower extremities of the different chains instead were fixed using the "setforce" command.

Finally, coming to the bond breaking used in chapter 7, it was implemented using *pyLAMMPS*, the *python* implementation of LAMMPS, in order to automatize the process. This in practice was done by deleting the interested bond and angles ("delete_bonds") and all the velocities.

```
1
2                 L.group(f"brok id {500+atom_bond_to_delete} {500+atom_bond_to_delete+1}
    ")
3                 L.group(f"brok_angle id {500+atom_bond_to_delete-1} {500+
    atom_bond_to_delete} {500+atom_bond_to_delete+1} {500+atom_bond_to_delete+2}")
4
5                 L.velocity("all set 0 0 0")
6                 L.delete_bonds("brok bond 1 remove")
7                 L.delete_bonds("brok_angle angle 1 remove")
```

Listing A.4: Generating bond breaking

In this case the variable "atom_bond_to_delete" referred to the position of the atom to delete.

Appendix B

DNA Topology

The knowledge of DNA topology is fundamental when discussing the DNA supercoiling. In order to describe the possible configurations and the properties of such winded molecules it is useful to introduce some topological descriptors. The first introduced parameter is called linking number and directly associated to the number of crossing in a closed curve made up by two strands. In both magnetic tweezers and simulated conditions it is possible in fact to obtain a closed curve by fixing the extremities of the dsDNAs (real and simulated) to the upper and bottom walls and rotating them to the desired configuration. The resulting structure topologically corresponds to a pair of closed strands, whose linking number can be calculated as:

$$Lk = \frac{1}{2}\sum_i w_i$$

Where $w_i = +1$ for a right-hand crossing and $w_i = -1$ for a left-hand crossing as shown in figure B.1, once chosen an orientation for the strands and projected their structure on a 2D plane.

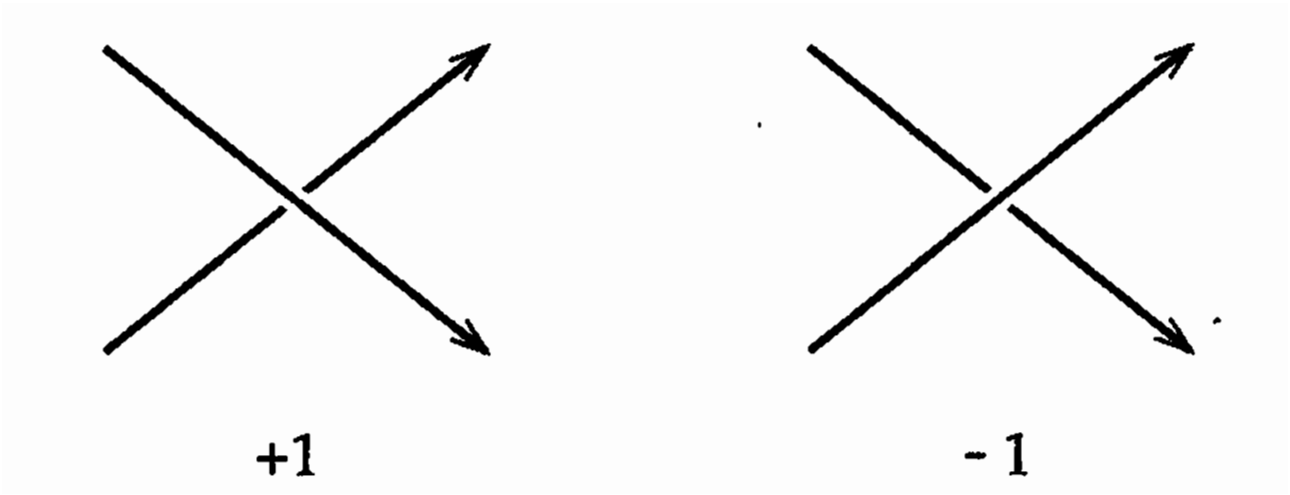

Figure B.1: Convention for linking number calculation, via [32].

Twist and writhe represent instead two different variables, associated to the contortion in space of the strands pair. Taking in fact the ribbon with borders represented by the two strands, the writhe can be associated to the axis contortion in space, being calculated as the sum of crossover numbers of the axis itself, according to the convention in figure B.1. The twist similarly can be calculated directly when the axis lies flat in the plane, being one-half of the sum of the crossing numbers (again, according to figure B.1) occurring at the crossings between the axis and one of the two strands, as it can be observed in figure B.2. When the axis lying condition is not respected the computation becomes more difficult, but the final value continues to represent how much of ribbon twist about the axis along the curve. These two values depend directly on the chosen projection, while their sum remains constant

and corresponds to the linking number between the two strands, representing a topological invariant of the system [32].

Figure B.2: Examples of twist and writhe calculations for a ribbon, via [32].

The computation of the writhe in particular is fundamental when dealing with supercoiled DNA, being associated to the self-crossing present in plectonemes. The computational calculation of its value on the coordinates obtained directly from LAMMPS files can be done computationally by discretizing the chosen strand and applying a Gauss integral on the sequence of vectors [33].

$$Wr = \frac{1}{4\pi}\int_{C_1}\int_{C_1}\frac{(d\vec{r}_2 \times d\vec{r}_1)\vec{r}_{12}}{r_{12}^3} \approx \frac{1}{4\pi}\sum_{C_1}\sum_{C_1}\frac{(\Delta\vec{r}_2 \times \Delta\vec{r}_1)\vec{r}_{12}}{r_{12}^3},$$

where C_1 represent the chosen curve, $\vec{r}_1$ and $\vec{r}_2$ the tangent vector for each position on the curve, and $\vec{r}_{12}$ the vector joining those points. The same formula can be used to get a computational estimate of the linking number if calculated on the two different strands.

$$Lk = \frac{1}{4\pi}\int_{C_1}\int_{C_2}\frac{(d\vec{r}_2 \times d\vec{r}_1)\vec{r}_{12}}{r_{12}^3} \approx \frac{1}{4\pi}\sum_{C_1}\sum_{C_2}\frac{(\Delta\vec{r}_2 \times \Delta\vec{r}_1)\vec{r}_{12}}{r_{12}^3}$$

The linking number for the 3-chains cases is calculated between each pair of chains, and corresponds to the catenation number of the studied simulation. This last value is the number of rotations that the upper wall underwent in order to get the chosen configuration.

Bibliography

[1] James D. Watson and Francis H. Crick. A structure for deoxyribose nucleic acid. *Nature*, 171:737–738, April 1953.

[2] Andrew Travers and Georgi Muskhelishvili. DNA structure and function. *FEBS Journal*, 282(12):2279–2295, June 2015.

[3] Berenike Maier, David Bensimon, and Vincent Croquette. Replication by a single DNA polymerase of a stretched single-stranded DNA. *Proceedings of the National Academy of Sciences*, 97(22):12002–12007, October 2000.

[4] C. D. Hardy, N. J. Crisona, M. D. Stone, and N. R. Cozzarelli. Disentangling DNA during replication: a tale of two strands. *Philos Trans R Soc Lond B Biol Sci*, 359(1441):39–47, Jan 2004.

[5] T.R. Strick, J.-F. Allemand, D. Bensimon, and V. Croquette. Behavior of supercoiled DNA. *Biophysical Journal*, 74(4):2016–2028, April 1998.

[6] James C. Wang. Cellular roles of DNA topoisomerases: a molecular perspective. *Nature Reviews Molecular Cell Biology*, 3(6):430–440, June 2002.

[7] J. E. Deweese, M. A. Osheroff, and N. Osheroff. DNA Topology and Topoisomerases: Teaching a "Knotty" Subject. *Biochem Mol Biol Educ*, 37(1):2–10, 2008.

[8] M. T. J. van Loenhout, M. V. de Grunt, and C. Dekker. Dynamics of dna supercoils. *Science*, 338(6103):94–97, 2012.

[9] Wilma K. Olson and Peisen Zhang. [21] computer simulation of DNA supercoiling. In *Methods in Enzymology*, pages 403–432. Elsevier, 1991.

[10] Brad A. Krajina and Andrew J. Spakowitz. Large-scale conformational transitions in supercoiled DNA revealed by coarse-grained simulation. *Biophysical Journal*, 111(7):1339–1349, October 2016.

[11] A. Ghatak and L. Mahadevan. Solenoids and plectonemes in stretched and twisted elastomeric filaments. *Phys. Rev. Lett.*, 95:057801, Jul 2005.

[12] G. Charvin, A. Vologodskii, D. Bensimon, and V. Croquette. Braiding dna: Experiments, simulations, and models. *Biophysical Journal*, 88(6):4124–4136, 2005.

[13] Sumitabha Brahmachari, Kathryn H. Gunn, Rebecca D. Giuntoli, Alfonso Mondragón, and John F. Marko. Nucleation of multiple buckled structures in intertwined dna double helices. *Phys. Rev. Lett.*, 119:188103, Oct 2017.

[14] Sumitabha Brahmachari and John F. Marko. Torque and buckling in stretched intertwined double-helix dnas. *Phys. Rev. E*, 95:052401, May 2017.

[15] I. D. Vilfan, J. Lipfert, D. A. Koster, S. G. Lemay, and N. H. Dekker. *Magnetic Tweezers for Single-Molecule Experiments*, pages 371–395. Springer US, New York, NY, 2009.

[16] Richard Janissen, Bojk A. Berghuis, David Dulin, Max Wink, Theo van Laar, and Nynke H. Dekker. Invincible DNA tethers: covalent DNA anchoring for enhanced temporal and force stability in magnetic tweezers experiments. *Nucleic Acids Research*, 42(18):e137–e137, August 2014.

[17] Giada Forte, Michele Caraglio, Davide Marenduzzo, and Enzo Orlandini. Plectoneme dynamics and statistics in braided polymers. *Phys. Rev. E*, 99:052503, May 2019.

[18] Ikenna D. Ivenso and Todd D. Lillian. Simulation of dna supercoil relaxation. *Biophysical Journal*, 110(10):2176–2184, 2016.

[19] A. P. Thompson, H. M. Aktulga, R. Berger, D. S. Bolintineanu, W. M. Brown, P. S. Crozier, P. J. in 't Veld, A. Kohlmeyer, S. G. Moore, T. D. Nguyen, R. Shan, M. J. Stevens, J. Tranchida, C. Trott, and S. J. Plimpton. LAMMPS - a flexible simulation tool for particle-based materials modeling at the atomic, meso, and continuum scales. *Comp. Phys. Comm.*, 271:108171, 2022.

[20] Carl P. Goodrich and Michael P. Brenner. Using active colloids as machines to weave and braid on the micrometer scale. *Proceedings of the National Academy of Sciences*, 114(2):257–262, 2017.

[21] G. Charvin, D. Bensimon, and V. Croquette. Single-molecule study of DNA unlinking by eukaryotic and prokaryotic type-II topoisomerases. *Proceedings of the National Academy of Sciences*, 100(17):9820–9825, August 2003.

[22] Job Ubbink and Theo Odijk. Electrostatic-undulatory theory of plectonemically supercoiled dna. *Biophysical Journal*, 76(5):2502–2519, 1999.

[23] A. Ashkin, J. M. Dziedzic, J. E. Bjorkholm, and Steven Chu. Observation of a single-beam gradient force optical trap for dielectric particles. *Opt. Lett.*, 11(5):288–290, May 1986.

[24] Rupa Sarkar and Valentin V. Rybenkov. A guide to magnetic tweezers and their applications. *Frontiers in Physics*, 4, December 2016.

[25] Iwijn De Vlaminck and Cees Dekker. Recent advances in magnetic tweezers. *Annual review of biophysics*, 41:453–72, 2012.

[26] Chris A. Brackey, Davide Marenduzzo, and Nick Gilbert. Mechanistic modeling of chromatin folding to understand function. *Nature Methods*, 17(8):767–775, June 2020.

[27] Kurt Kremer and Gary S. Grest. Erratum: Dynamics of entangled polymer melts: A molecular-dynamics simulation [j. chem. phys. 92, 5057 (1990)]. *The Journal of Chemical Physics*, 94(5):4103–4103, 1991.

[28] Alan D. Sokal. Monte carlo methods in statistical mechanics: Foundations and new algorithms. 1996.

[29] Joseph L Sleiman, Robin H Burton, Michele Caraglio, Yair Augusto Gutierrez Fosado, and Davide Michieletto. Geometric predictors of knotted and linked arcs, 2022.

[30] Håkan Wennerström and Ulf Olsson. Microemulsions as model systems. *Comptes Rendus Chimie*, 12(1):4–17, 2009. Matière molle et chimie : un mélange fructueux.

[31] Guido Van Rossum and Fred L. Drake. *Python 3 Reference Manual*. CreateSpace, Scotts Valley, CA, 2009.

[32] C.C. Adams. *The Knot Book*. W.H. Freeman, 1994.

[33] Konstantin Klenin and Jörg Langowski. Computation of writhe in modeling of supercoiled dna. *Biopolymers*, 54(5):307–317, 2000.